

RESEARCH ARTICLE

10.1002/2015JB012551

This article is a companion to *Dempsey and Suckale* [2016] doi:10.1002/2015JB012550.

Key Points:

- Induced seismicity b value evolution reflects modification of underlying rupture energy physics
- Deficit of induced large-magnitude events due to a plume shape effect
- Guy, AR seismicity model of rate, migration, nonlinear GR distribution; invert fault permeability

Correspondence to:

D. Dempsey, ddempsey786@gmail.com

Citation:

Dempsey, D., J. Suckale, and Y. Huang (2016), Collective properties of injection-induced earthquake sequences: 2. Spatiotemporal evolution and magnitude frequency distributions, *J. Geophys. Res. Solid Earth*, 121, doi:10.1002/2015JB012551.

Received 23 SEP 2015

Accepted 10 APR 2016

Accepted article online 22 APR 2016

Collective properties of injection-induced earthquake sequences: 2. Spatiotemporal evolution and magnitude frequency distributions

David Dempsey^{1,2}, Jenny Suckale¹, and Yihe Huang¹

¹Department of Geophysics, Stanford University, Stanford, California, USA, ²Now at Department of Engineering Science University of Auckland, Auckland, New Zealand

Abstract Probabilistic seismic hazard assessment for induced seismicity depends on reliable estimates of the locations, rate, and magnitude frequency properties of earthquake sequences. The purpose of this paper is to investigate how variations in these properties emerge from interactions between an evolving fluid pressure distribution and the mechanics of rupture on heterogeneous faults. We use an earthquake sequence model, developed in the first part of this two-part series, that computes pore pressure evolution, hypocenter locations, and rupture lengths for earthquakes triggered on 1-D faults with spatially correlated shear stress. We first consider characteristic features that emerge from a range of generic injection scenarios and then focus on the 2010–2011 sequence of earthquakes linked to wastewater disposal into two wells near the towns of Guy and Greenbrier, Arkansas. Simulations indicate that one reason for an increase of the Gutenberg-Richter b value for induced earthquakes is the different rates of reduction of static and residual strength as fluid pressure rises. This promotes fault rupture at lower stress than equivalent tectonic events. Further, b value is shown to decrease with time (the induced seismicity analog of b value reduction toward the end of the seismic cycle) and to be higher on faults with lower initial shear stress. This suggests that faults in the same stress field that have different orientations, and therefore different levels of resolved shear stress, should exhibit seismicity with different b -values. A deficit of large-magnitude events is noted when injection occurs directly onto a fault and this is shown to depend on the geometry of the pressure plume. Finally, we develop models of the Guy-Greenbrier sequence that captures approximately the onset, rise and fall, and southwest migration of seismicity on the Guy-Greenbrier fault. Constrained by the migration rate, we estimate the permeability of a 10 m thick critically stressed basement fault to be 5×10^{-12} m². We also consider alternative scenarios in which only one of the two disposal wells operated and suggest that, due to the wells interacting, total seismicity may be greater than that attributable to each well alone.

1. Introduction

Underground fluid injection has the potential to induce earthquakes on critically stressed faults [Healy et al., 1968; Raleigh et al., 1976; Zoback and Harjes, 1997]. Such earthquakes represent a financial and public safety hazard when performing wastewater disposal [e.g., Horton, 2012; Keranen et al., 2013], well stimulation to create an Enhanced Geothermal System (EGS) [e.g., Häring et al., 2008] and geologic storage of carbon dioxide [Zoback and Gorelick, 2012].

Probabilistic Seismic Hazard Analysis (PSHA) [Cornell, 1968] provides a framework for quantifying earthquake hazard from ground acceleration. An important step in PSHA is characterizing the rates at which earthquakes of different magnitudes are expected to occur. For tectonic earthquakes, the seismicity rate can be regarded as quasi-constant because it depends on tectonic plate motions that vary on timescales much longer than those considered by the risk assessment. The magnitude frequency distribution is often described by the Gutenberg-Richter (GR) model, which is expressed as

$$\log N(M) = a - b(M - M_{\min}) \tag{1}$$

where $N(M)$ is the number of events with magnitude greater than or equal to M , 10^a is the total number of events larger than M_{\min} , and the so-called b value controls the relative number of small- to large-magnitude

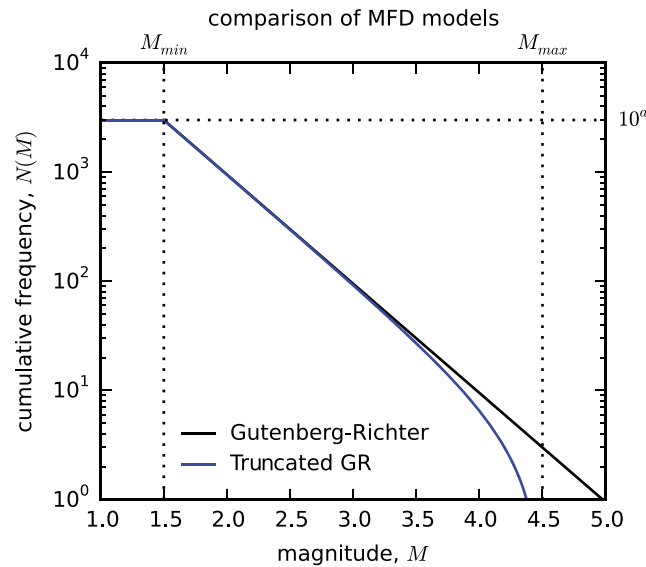


Figure 1. Comparison of Gutenberg-Richter (GR) and Truncated GR models. For this illustration, the lower magnitude cutoff, M_{min} , is 1.5, the upper magnitude cutoff, M_{max} , is 4.5; the catalog contains 3000 events, i.e., $a = \log 3000 \approx 3.5$, and $b = 1$.

eluting features of induced seismicity that are strongly dependent on the specific heterogeneity at a site, e.g., the timing of the largest magnitude event.

In PSHA, it is sometimes useful to use a truncated form of (1) that accounts for an upper magnitude limit, M_{max} , imposed by the length of the fault [Utsu, 1999]

$$\log N(M) = a - \log \left(\frac{10^{-b(M-M_{max})} - 1}{10^{-b(M_{min}-M_{max})} - 1} \right). \quad (2)$$

The effect of an upper magnitude limit is to introduce convexity at high magnitude in the magnitude frequency distribution (Figure 1). In the limit that $M \ll M_{max}$, (2) reduces to (1).

Sometimes, the magnitude frequency distribution for induced earthquakes exhibits convexity at the large-magnitude limit [e.g., Dorbath et al., 2009; Friberg et al., 2014; Cesca et al., 2014; Huang and Beroza, 2015]. Shapiro et al. [2011] model this convexity by considering a statistical model for rupture with an M_{max} emerging from an imposed limit on rupture length by the finite size (L_{max}) of an ellipsoidal stimulation volume. The concept of an upper limit to M_{max} imposed by the finite volume of the fluid-perturbed zone is also invoked by McGarr [2014] who formulates M_{max} in terms of both the volume of injected fluid and the elastic properties of the crust. These approaches exclude the possibility of large-magnitude events propagating beyond the region of the fault where pressure is elevated. This shortcoming is addressed in a modeling study by Gischig [2015] who delineates two regimes of rupture—pressure front limited and uncontrolled—depending on the level of shear stress on the fault. It should be noted that M_{max} imposed by the dimensions of a pressure plume is not the same as that imposed by the finite size of a fault, which will always be larger.

Another property of the magnitude frequency distribution that is sometimes used to distinguish induced and natural earthquakes is the b value. While measurement of the b value depends on the magnitude scale and the method of fitting a GR model, consistent trends have nevertheless emerged across a range of induced seismicity case studies. For example, values as high as 2.0 are observed during hydraulic fracturing of shales, between 1.2 and 1.6 during EGS well stimulation, and between 1.4 and 2.0 for natural gas and CO₂ injection (see Table 1 for locations and references). In some instances [Gibbs et al., 1973; Ake et al., 2005; Brodsky and Lajoie, 2013; Holland, 2013; Friberg et al., 2014; Skoumal et al., 2015], there is no clear indication that the b value is different from the range associated with tectonic seismicity (0.8 to 1.2) [from Schorlemmer et al., 2005]. In other instances of wastewater disposal, a depression of the b value is observed during periods of injection [Lei et al., 2008, 2013; Huang and Beroza, 2015; Goebel et al., 2016].

events. Observations of tectonic earthquakes suggest that b varies in the range 0.8 to 1.2 [Schorlemmer et al., 2005] with a worldwide average close to 1.0 [El-Isa and Eaton, 2014].

In several modeling studies, GR scaling of the magnitude frequency distribution is replicated through spatial heterogeneity of stress or strength [e.g., Huang and Turcotte, 1988; Zöller et al., 2005; Ampuero et al., 2006; Murphy et al., 2013]. One of the key features of the model we use here is a stochastic description of fault stress heterogeneity from which we show that GR scaling is an emergent property. The advantage of this stochastic approach is that it averages over the geological uncertainty and heterogeneity associated with specific events so that we can focus on the collective properties of the earthquake catalog. However, the approach is not suitable for mod-

Table 1. Summary of Induced Seismicity b Values Reported in the Literature^a

Activity	Location	b Value	Reference
HF - ↑	Attica Dale, New York, USA	1.1–1.5	<i>Fletcher and Sykes</i> [1977]
HF - ↑	Barnett shale, USA	1.5–1.9	<i>Vermilyen and Zoback</i> [2011]
	Other shales	1.8–2.0	<i>Zhou et al.</i> [2013]
		1.9	<i>Guest et al.</i> [2014]
EGS - ↑	Basel, Switzerland	1.1–1.6	<i>Bachmann et al.</i> [2012]
EGS - ↑	Soultz, France	1.2	<i>Dorbath et al.</i> [2009]
EGS - ↑	Paralana, Australia	1.3	<i>Albaric et al.</i> [2014]
NGS - ↑	Puhagan, Philippines	1.3	<i>Bromley et al.</i> [1987]
GI - ↑	Offshore Spain	1.4	<i>Cesca et al.</i> [2014]
GI - ↑	In Salah, Algeria	1.5–2.0	<i>Goertz-Allmann et al.</i> [2014]
WD - ↑	Dallas-Fort Worth, Texas, USA	1.3	<i>Frohlich et al.</i> [2011]
WD - ↑ and ↓	Sichuan Basin, China	0.8–1.3	<i>Lei et al.</i> [2008]
		0.7–1.4	<i>Lei et al.</i> [2013]
WD - ↓	Guy, Arkansas, USA	0.8	[<i>Huang and Beroza</i> , 2015], this study

^aHF = Hydraulic Fracturing, EGS = Enhanced Geothermal System, NGS = Natural Geothermal System, GI = Gas Injection, WD = Wastewater Disposal, ↑ = b value higher than tectonic range, ↓ = b value lower than tectonic range.

In microfracturing experiments, elevated b values are observed at low levels of shear stress [Scholz, 1968]. Earthquake observations in different tectonic regimes are consistent with these small-scale experiments: b values tend to be elevated in extensional regimes where shear stress (at a given depth) is lower and depressed in compressional ones where shear stress is higher [Schorlemmer et al., 2005]. Scholz [1968] explain this relationship using a heterogeneity model for fracture shear stress and propose that higher levels of stress increase the likelihood that small ruptures will grow into larger ones. Based on this idea, Bachmann et al. [2012] and Goertz-Allmann and Wiemer [2013] develop a stochastic model of induced seismicity in which fractures are seeded throughout a volume with a randomly assigned value of differential stress, σ_d , from a prescribed normal distribution and, upon failing, are assigned an event magnitude sampled from a GR distribution in which the b value is a prescribed linear function of σ_d . Their model reproduces elevated b value near the injection well where pressures are high enough to activate fractures with low σ_d (and thus high b value). Assuming that stress drop is proportional to shear stress, their model also reproduces observations of low stress drop near the injection well [Goertz-Allmann et al., 2011; Lengliné et al., 2014]. The model we use extends the theoretical framework of Scholz [1968] to specific spatial heterogeneity and distribution functions and the stochastic model of Bachmann et al. [2012] and Goertz-Allmann and Wiemer [2013] to include a physical description of the rupture process and event size.

An elevated b value corresponds to a magnitude frequency distribution with relatively more low-magnitude events. Earthquake magnitude depends on rupture length, L , through the seismic moment, M_0 [Aki, 1972]. In this study, we consider ruptures on 1-D faults with heterogeneous stress drop, for which M_0 is given [Madariaga, 1979]

$$M_0 = L^2 \int_{-1}^1 \Delta\tau(z) \sqrt{1-z^2} dz = L^2 \Delta\bar{\tau}, \quad (3)$$

where $\Delta\tau$ is the heterogeneous stress drop distribution, $\Delta\bar{\tau}$ is the average stress drop assuming an elliptical distribution of slip [Eshelby, 1957], and z is a dimensionless coordinate spanning the rupture. Strictly speaking, equation (3) gives the moment per length in the out-of-plane direction. However, for true 1-D ruptures—i.e., in a universe with only two space dimensions—there is no concept of an out-of-plane direction and (3) fully describes seismic moment.

Incorporating (3) into the moment magnitude definition [Hanks and Kanamori, 1979], we write magnitude as

$$M_W = \frac{4}{3} \log(L^*) + \log\left(\frac{\Delta\bar{\tau}}{\Delta\bar{\tau}_{\text{ref}}}\right) + M_{W,0}, \quad (4)$$

where $L^*(= L/L_0)$ is the rupture length nondimensionalized by the length of the fault, L_0 , and $M_{W,0}$ is a reference event magnitude corresponding to full fault rupture and a reference stress drop, $\Delta\bar{\tau}_{\text{ref}}$.

An alternative approximation of event magnitude is obtained by assuming the existence of an out-of-plane dimension, e.g., when rupture occurs on a 2-D fault. In this case, to avoid extreme and unphysical rupture aspect ratios, it is common to assume that the out-of-plane dimension is proportional to L^* , which recovers the more familiar form $M_w = 2 \log L^* + \text{const}$. Here we aim for maximum consistency with the concept of 1-D fault rupture and use the form (4). However, a degree of conservatism is necessary when interpreting results in the context of more realistic 2-D ruptures and, for this reason, conclusions drawn tend to be qualitative in nature.

Fixing for now $\Delta \bar{\tau}$, one can use (4) to perform a distribution change of variables on (1) and obtain the GR model for L

$$\log N(L) = a - \frac{4b_L}{3} \log(L/L_{\min}) \quad (5)$$

where L_{\min} is the rupture length corresponding to M_{\min} , $N(L)$ is the number of events with rupture length greater than L , and b_L is a b value that explicitly neglects the effect of stress drop on the magnitude frequency distribution. In this form, we can consider the implication for b value of various transformations of the rupture length distribution. Transforming L by a fixed power, α , e.g., $L \rightarrow L^\alpha$, scales the b value by a factor $1/\alpha$, whereas a linear transformation, e.g., $L \rightarrow \gamma L$, does not alter the b value. Thus, one explanation for shifted b values associated with induced seismicity is that there might be a preference for smaller rupture lengths resulting in a power law transformation of the underlying length distribution. The goal of this paper is to investigate the interaction between injection and the rupture process that might cause this effect.

This paper is organized as follows: section 2 summarizes the key features of the earthquake sequence model developed in part one, including governing equations, reservoir and rupture simulation, and the stochastic fault stress model. In section 3, we investigate how parameters of the stress model influence the magnitude frequency distribution of earthquake catalogs simulated under a tectonic loading condition and establish parameters that reproduce GR scaling. In section 4.1, we consider induced seismicity caused by uniform pressure rise on a fault and investigate variations of the GR b value. In section 4.2, we introduce asymmetry to the pressure plume and consider a wider range of injection parameters. Finally, in section 5, we apply our model to a sequence of earthquakes in Arkansas in 2010–2011 that were likely induced by wastewater injection at two wells. In particular, we focus on the spatiotemporal evolution of seismicity and how things might have been different if only one well had been operating.

2. Model Description

Here we summarize the main features of our model for induced seismicity, which is developed in the first paper in this two-part series. The model combines a description of heterogeneous shear stress on 1-D faults, reservoir simulations of injection and fault pressure evolution, and the physics of fault rupture conceptualized as an expanding bilateral crack. The model outputs an ensemble of fault ruptures—representing an earthquake catalog—each of which is characterized by a hypocenter location, rupture length, and event time. Symbols and acronyms used in the text are summarized in Table 2.

The 1-D fracture mechanics model is attractive because its reduced computational expense enables simulation of large earthquake catalogs. Nevertheless, care must be exercised in interpreting model results and their implications for real earthquakes on 2-D faults. The main limitation is an absence of 2-D effects, e.g., rupture propagation around barriers. Nevertheless, previous studies have used similar 1-D models to replicate a range of earthquake behavior [Ampuero *et al.*, 2006; Ampuero and Ben-Zion, 2008; Kammer *et al.*, 2015] and, as we show here and in the first paper, our model also generates seismicity with directivity and magnitude frequency properties consistent with seismological observation. We take a conservative approach to interpreting insights gained from the 1-D model and adopt a view that qualitative agreement between 1-D model and 2-D reality is reasonable when 2-D effects are expected to be minimal.

In part one, we defined the nondimensional spatial, x^* , and temporal scales, t^* , evolving pressure distribution on the fault, ΔP^* , static and residual shear strength, τ_s^* and τ_r^* , and the potential stress drop, $\tau^* = \tau_0^* + \Delta P^*$, where τ_0^* is the spatially variable shear stress on the fault (see Table 3 for a summary of these quantities). It is important to reiterate that the nondimensional stress, τ^* , reflects the difference between shear stress, τ_0 , and a residual strength, τ_r , which has potentially been reduced by fluid overpressure. This reduction modifies the

Table 2. Table of Symbols and Acronyms^a

Symbol/Acronym	Meaning
a, b	GR productivity, magnitude frequency parameter
C_r	Pressurization/criticality ratio
C_v	Curvature of magnitude frequency distribution
L, L_0	Rupture, fault length
n	Fractal exponent
$N(M)$	Number of earthquakes with magnitude larger than M
\dot{N}	Seismicity rate
M, M_{\min}, M_{\max}	Earthquake magnitude, minimum, maximum in truncated GR model
$M_{W,0}$	Upper magnitude limit on the fault
P_0	Pore pressure
$\Delta P, \Delta P_{\text{inj}}$	Overpressure, value applied at injector
ΔP_{max}	Overpressure causing tensile failure
t_h	Earthquake time
x_h	Earthquake location (hypocenter)
κ_f	Fault permeability
μ_τ	Mean of stress PDF
σ_τ	Standard deviation of stress PDF
$\tau, \bar{\tau}$	Shear stress, average on fault
τ_s, τ_r	Static strength, residual
ANSS	Advanced National Seismic System
EGS	Enhanced Geothermal System
ETAS	Epidemic Type Aftershock Sequence
GGS	Guy-Greenbrier Sequence catalog
GR	Gutenberg-Richter
PDF	Probability Density Function
PSHA	Probabilistic Seismic Hazard Assessment
RS	Rate-and-State
TR0	Tectonic Reference catalog
UPR	Uniform Pressure Rise catalog
UPR-E	Uniform Pressure Rise catalog with ETAS events
WHAR	Station in the Arkansas Seismic Network

^aStarred symbols (*) refer to dimensionless quantities. Stress variables with the subscript 0 refer to quantities when $\Delta P=0$.

energetics of fault rupture. The actual stress drop is computed over the section of the fault that ruptures and is therefore different to the potential stress drop.

The nondimensional seismicity rate, \dot{N}^* , is defined

$$\dot{N}^* = \frac{1}{N_{\text{tot}}} \frac{N(t_{i-1}^* < t_h^* < t_i^*)}{t_i^* - t_{i-1}^*}, \quad (6)$$

where $N(t_{i-1}^* < t_h^* < t_i^*)$ is the number of modeled events with event time, t_h^* , in the interval $[t_{i-1}^*, t_i^*]$, and N_{tot} is number of faults in the ensemble.

2.1. Model Physics

Heterogeneous shear stress, τ_0^* , on a fault is described by a fractal model in which the Fourier amplitude spectrum of stress is given by a power law, i.e., $|\tilde{\tau}_0^*(k)| \propto k^{-n}$, where the tilde indicates a Fourier transform, k is the spatial wave number, and n is the fractal exponent. Spatially correlated 1-D profiles of τ_0^* have values drawn from a positively skewed Gumbel probability density function (PDF) with mean, μ_τ^* and standard deviation, σ_τ^* . Respectively, these parameters capture the level of stress on the fault and the relative amount of roughness in the stress profile.

Table 3. Summary of Nondimensional Quantities Used in the Text^a

$$x^* = x/L_0 \quad (7)$$

$$t^* = \frac{\rho g \kappa_f}{\eta L_0} t \quad (8)$$

$$\Delta P^* = \frac{f_r \Delta P}{\tau_{s,0} - \tau_{r,0}} \quad (9)$$

$$\tau_r^* = \frac{\tau_r - \tau_{r,0}}{\tau_{s,0} - \tau_{r,0}} = -\Delta P^* \quad (10)$$

$$\tau_s^* = \frac{\tau_s - \tau_{r,0}}{\tau_{s,0} - \tau_{r,0}} = 1 - \frac{f_s}{f_r} \Delta P^* \quad (11)$$

$$\tau^* = \frac{\tau - \tau_r}{\tau_{s,0} - \tau_{r,0}} = \tau_0^* + \frac{f_s}{f_r} \Delta P^* \quad (12)$$

$$\Delta P_{\max}^* = \frac{f_r}{f_s - f_r} \quad (13)$$

$$C_r = \Delta P_{\text{inj}}^* / (1 - \mu_\tau^*) \quad (14)$$

$$\mu_\tau^* = \mu_{\tau,0}^* \left(1 - \frac{f_s - f_r}{f_r} \Delta P^* \right) - \Delta P^* \quad (15)$$

$$\sigma_\tau^* = \sigma_{\tau,0}^* \left(1 - \frac{f_s - f_r}{f_r} \Delta P^* \right) \quad (16)$$

^aSee first paper in this two-part series for derivations. L_0 = length of fault, ρ = fluid density (10^3 kg m^{-3}), η = fluid viscosity ($8.9 \times 10^{-4} \text{ Pa s}$), g = acceleration of gravity, κ_f = permeability of fault, f_r = residual friction coefficient, f_s = static friction coefficient, ΔP = fluid pressure change, $\tau_{s,0}$ = initial static strength, τ_s = fluid pressure modified static strength, $\tau_{r,0}$ = initial residual strength, τ_r = fluid pressure modified residual strength, τ = shear stress, ΔP_{\max} = fluid pressure change at which tensile failure occurs, $\mu_{\tau,0}^*$ = value of μ_τ^* when $\Delta P^* = 0$. Starred symbols (*) refer to dimensionless quantities.

($\tau^* < 0$, where stress is less than residual strength, acting as an energy sink), and fracture energy. Note, as τ^* includes both shear stress and fluid pressure contributions, the pressure distribution modifies rupture energetics. Comparison of the simplified crack model against fully dynamic rupture simulations on faults with heterogeneous stress indicate that L^* is overestimated by on average 16% (because interactions between the two propagating tips are neglected) with larger overestimate and underestimate occurring infrequently.

The three steps for simulating an induced earthquake rupture are then (Figure 2, see part one for additional details) (1) construct a realization of $\tau_0^*(x^*)$ for given stress parameters [n , σ_τ^* , μ_τ^*]; (2) compute $\Delta P^*(x^*, t^*)$ for a given flow parameters [geometry, κ_f , ΔP_{inj}^*] and use the Mohr-Coulomb failure criterion to calculate t_h^* and x_h^* ; and (3) estimate L^* using the crack tip equation of motion for prescribed static, f_s , and residual friction coefficients, f_r , and fracture energy, Γ^* .

Modeled earthquake catalogs comprise a collection of ruptures modeled on an ensemble of faults, each with a different realization of τ_0^* , constructed from the same stochastic stress model. Pressure evolution, $\Delta P^*(x^*, t^*)$ and friction properties are the same for all faults. This is an average representation of an earthquake sequence and will not capture features or behavior attributable to the specific realization of shear stress heterogeneity on a real-world fault. A stochastic approximation of fault stress evolution is employed to model sustained periods of induced seismicity. The complete catalog is imagined as comprising a collection of subcatalogs, each of which is an ensemble of faults with a nonuniform mean stress that reflects the nonuniform pressure-induced strength drop. The final catalog is a weighted sum of all subcatalogs, with the event weights computed such that the simulated seismicity (total stress drop) is spatiotemporally consistent with the prescribed stress evolution (total strength drop).

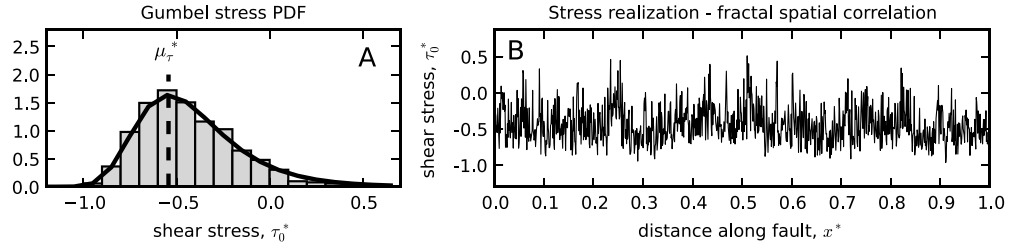
3. Magnitude Frequency Properties of Modeled Tectonic Earthquakes

As in part one, we first simulate a catalog of earthquakes approximating tectonic seismicity, designated catalog TR0 (Tectonic Reference). For the purposes of this paper, TR0 serves as a benchmark against which to compare modeled magnitude frequency properties of induced seismicity. It also allows us to calibrate the fractal stress model. The loading condition for modeled tectonic events is uniform shear stress increase

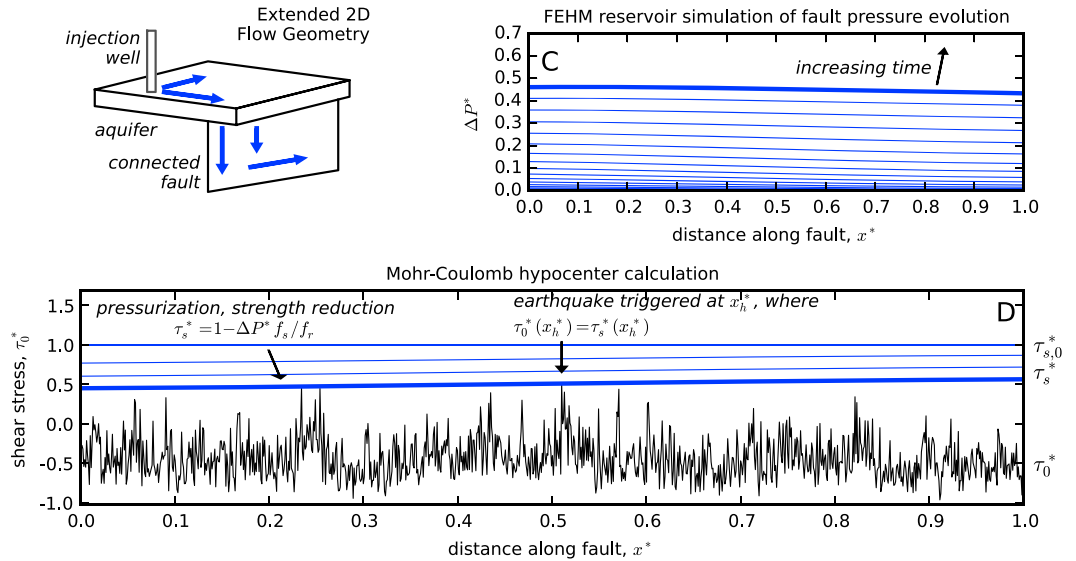
Two scenarios of injection and pressure evolution on a fault are simulated in the subsurface flow code FEHM [Zyvoloski, 2007], which solves for mass conservation in a porous medium subject to Darcy flow, uses rational functions to describe the pressure and temperature dependence of fluid density and viscosity, and assumes constant porosity and permeability. A third scenario prescribes a simple analytic model of pressure evolution. The three scenarios are as follows: 2-D radial flow, as occurs when an injection well intersect a fault; extended 2-D flow, describing wastewater disposal in an aquifer, causing seismicity on a basement fault; and an advancing step function approximating coevolution of a front of permeability enhancement and high pressure. Depending on the scenario, ΔP^* is sensitive to fault permeability, κ_f , injection pressure, ΔP_{inj}^* , and location of the injection well.

For a fault with heterogeneous shear stress, $\tau_0^*(x^*)$, and injection that results in evolving pressure distribution, $\Delta P^*(x^*, t^*)$, both catalog time, t_h^* , and earthquake hypocenter location, x_h^* , are determined by the Mohr-Coulomb criterion. Rupture length, L^* , is then estimated by a fracture mechanics approximation of a bilaterally expanding, semiinfinite crack [Eshelby, 1969] centered at x_h^* . This treats the rupture process as an energy balance between regions of positive ($\tau^* > 0$, energy sources) and negative potential stress drop

Step 1: Setup Heterogeneous, Spatially-Correlated Fault Stress Profile



Step 2: Earthquake Triggering - Calculate Hypocenter Location



Step 3: Earthquake Propagation - Calculate Rupture Extent

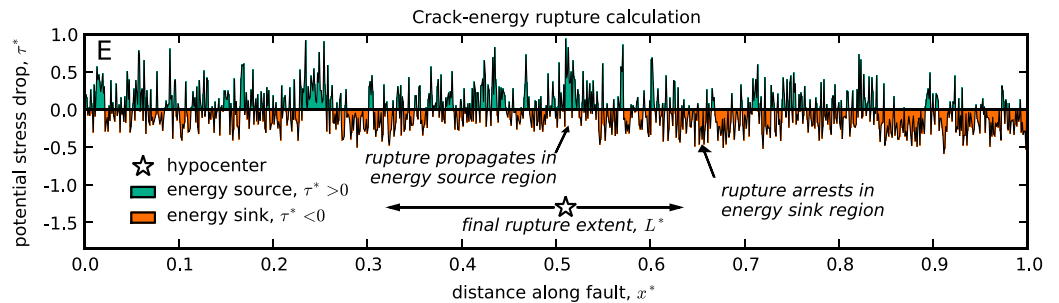


Figure 2. Summary of steps for modeling a single induced earthquake: (1) heterogeneous fault stress setup, (2) hypocenter calculation, and (3) rupture calculation. (a) Gumbel stress PDF characterizing the shear stress profile. (b) A particular realization of spatially correlated shear stress, τ_0^* , generated from a fractal $k^{-0.25}$ stress model. (c) Time evolution of pressure rise, ΔP^* , on the fault for the extended 2-D flow geometry. (d) Earthquake hypocenter calculated by successive reductions of the static strength, τ_s^* , until Mohr-Coulomb criterion, $\tau_0^* = \tau_s^*$, is satisfied (here $x_h^* = 0.51$). (e) Extent of fault rupture, L^* , determined by rupture arrest location of two crack tips expanding outward from x_h^* . Here rupture arrests at $x^* = 0.32$ and 0.64 .

representing the effects of far-field plate motion. Therefore, if the initial stress is $\tau_0^*(x^*)$, then the average potential stress drop on the fault (the average level of stress) at the time of failure will be

$$\bar{\tau}^* = \bar{\tau}_0^* + \Delta \tau_{\text{fail}}^*, \quad \Delta \tau_{\text{fail}}^* = \tau_s^* - \max(\tau_0(x^*)). \quad (17)$$

where $\Delta \tau_{\text{fail}}^*$ is the shear stress increase necessary to trigger an earthquake. As for part one, earthquakes are simulated for a fault with effective normal stress, $\sigma_n - P_0 = 40$ MPa, $f_s = 0.64$, and $f_r = 0.55$.

3.1. Constructing the Magnitude Frequency Distribution

The magnitude of modeled events is estimated by equation (4) using the modeled rupture length, L^* , and stress drop, $\Delta\bar{\tau}^*$. For the purposes of visualization, we set $M_{W,0} = 4.5$, which is within the range of interest for induced earthquakes, and $\Delta\bar{\tau}_{\text{ref}}^* = 0.1$. We require that modeled ruptures span at least five nodes. Thus, for the 1024 node fault discretization used in this study, the minimum resolvable event magnitude is 1.4 (for $\Delta\bar{\tau}^* = \Delta\bar{\tau}_{\text{ref}}^*$). As discussed in part one, discretization affects the resolution of model results, in this case the range of the magnitude frequency distribution, but not the accuracy.

We use the bootstrap sampling procedure discussed in Appendix A to construct a representation of the magnitude frequency distribution. The procedure uses random draws from the original catalog to produce a number of subcatalogs, constructs a magnitude frequency distribution, and fits a GR model for each, and then estimates ensemble statistics of the GR model parameters, e.g., b value. This procedure removes a finite fault effect that has the potential to obscure other modifiers to the shape of the magnitude frequency distribution that are the topic of investigation. It also quantifies variability of the magnitude frequency distribution at the large-magnitude limit where the statistics of small numbers dominate (Figure A1b).

3.2. Effect of Spatial Correlation

Spatial correlation in the shear stress profile is parameterized by the fractal exponent, n , which describes the power law dependence of the stress amplitude spectrum in the wave number domain. Increasing n has the effect of strengthening long-range correlations in shear stress by increasing spectral content at low spatial frequencies (Figure 3a). As the likelihood of stress correlation over a large area increases, high stress locations ($\tau^* > 0$) at which a rupture nucleates will increasingly support growth of the rupture into a larger event because the immediate vicinity will be biased (by virtue of the spatial correlation) toward positive stress drop. Thus, increasing the fractal exponent favors large-magnitude events and introduces convexity in the middle of the magnitude frequency distribution. This convexity is a substantial departure from the log-linear shape of most reported magnitude frequency distributions. To aid in identification of GR scaling in simulated distributions, it is useful to introduce a curvature parameter, C_v , which is an approximate measure of the departure from linearity (Appendix B). We have used $C_v < 0.45$ as an approximate criterion for a distribution that is close enough to linear that we may approximate it with a GR model (equation (1)).

Huang and Turcotte [1988] consider fractal distributions of stress on 2-D faults and obtain GR scaling for n between 2.2 and 2.4. However, their model of the rupture process does not account for stress transfer due to slip and the ability of a propagating rupture to penetrate regions of negative stress drop. These processes favor a larger rupture area and, when they are accounted for, a reduced degree of spatial correlation (smaller n) is required to reproduce GR scaling.

Our model produces a log-linear magnitude frequency distribution when $n = 0.25$. For comparison, *Smith and Heaton* [2011] used a fractal stress model to compare synthetic focal mechanisms with a catalog from southern California and obtained a best fit for n of 0.8. Another estimate of n is obtained from the following reasoning: (1) the fractal exponent for coseismic stress drop, n , is related to the fractal exponent of coseismic slip n_{slip} , as $n = n_{\text{slip}} - 1$ [*Andrews*, 1980], (2) *Mai and Beroza* [2002] analyzed 44 fault slip inversions for large earthquakes and obtained a median value for n_{slip} of 1.7, implying (3) that the median value for n is 0.7. This reasoning assumes that the present state of shear stress reflects the cumulative effect of many earthquakes and associated fractal stress drops.

The discrepancy between observations of n on 2-D faults in the range 0.7 to 1.0 and our use of a value of 0.25 is necessary for a power law distribution of magnitudes to emerge from the model. Clearly, our model does not incorporate the physics that lead to GR scaling for $n \sim 1$. One potential deficiency is our use of a constant fracture energy, Γ . Increasingly, there is evidence that Γ scales with the size of rupture [*Abercrombie and Rice*, 2005; *Causse et al.*, 2013], which would tend to discourage growth of small rupture into large ones (this is the opposite to what occurs as spatial correlation is increased at higher n). Another deficiency is the inability of a 1-D fault model to describe inherently 2-D effects, principally the propagation of a rupture around low stress barriers. Finally, recalling that we are investigating GR scaling on 1-D faults, the extent to which observations of n on 2-D faults can be used to constrain a 1-D model is unclear. As GR scaling and deviations from it are the topic of investigation here, we proceed with $n = 0.25$.

3.3. Factors Affecting the b Value

Equation (4) expresses magnitude in terms of rupture length and stress drop. Observations indicate that stress drop is not strongly magnitude dependent [*Abercrombie*, 1995], in which case the power law distribution of

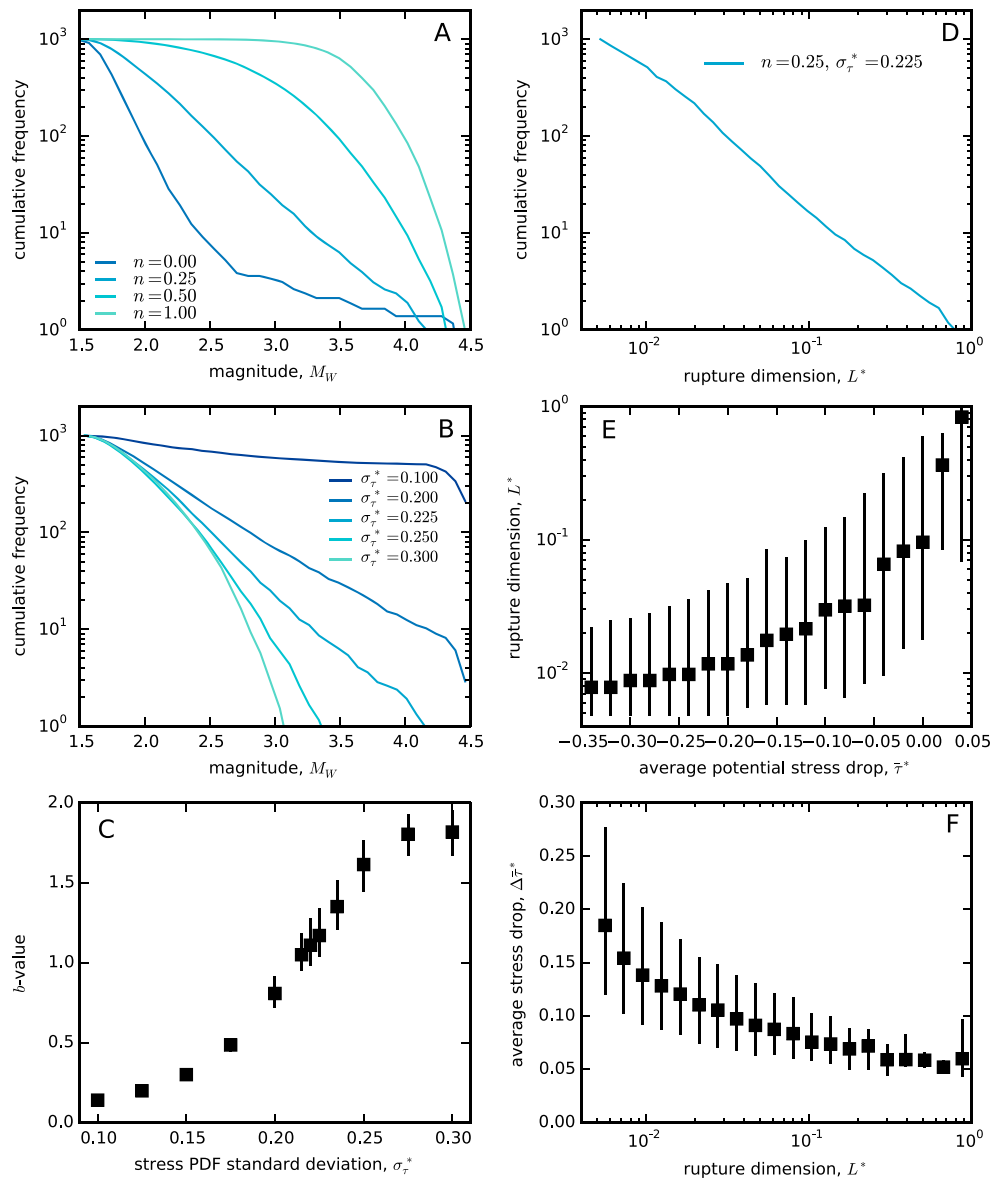


Figure 3. Sensitivity of the tectonic magnitude frequency distribution to parameters of the heterogeneous stress model: (a) Fractal exponent, n , fixing $\sigma_{\tau}^* = 0.225$ and (b) stress PDF standard deviation, σ_{τ}^* , fixing $n = 0.25$. (c) For the curves in Figure 3b (and other values of σ_{τ}^*), b value for a fitted GR model is plotted. Computation of b values along with their errors is described in Appendix A. For catalog TR0 with $n = 0.25$ and $\sigma_{\tau}^* = 0.225$, the b value is 1.15. (d) Cumulative frequency distribution of rupture length, L^* , for catalog TR0. (e) For all events in TR0, average (squares) and 5th–95th percentile range of L^* at different average potential stress drop, $\bar{\tau}^*$. (f) For all events in TR0, average (squares) and 5th–95th percentile range of average stress drop, $\Delta\bar{\tau}^*$, at different L^* .

M_W largely reflects an underlying power law distribution of L^* as seen in Figure 3d. Fitting equation (5) to this curves yields a value $b_L = 1.05$, which is smaller than the b value ~ 1.15 for the corresponding curve in Figures 3a and 3b and equation (5). The difference is attributed to the stress drop term, $\Delta\bar{\tau}^*$, in equation (4). Average stress drop shows a weak negative relationship with rupture length (Figure 3f). A similar relationship is observed by *Ampuero et al.* [2006] and they relate this to nucleation of events in regions of high stress.

Thus, if power law scaling of M_W reflects an underlying power law scaling of L^* , what controls the size of rupture and its distribution across many realizations? Figure 3e shows the range of L^* obtained for faults at different levels of stress as parameterized by the average potential stress drop, $\bar{\tau}^*$ (the difference between stress and residual strength). While $\bar{\tau}^*$ is not a unique predictor for L^* —the specific spatial correlation of a given realization plays a role as well—at higher values, it tends to produce ruptures that are more difficult to

Table 4. Modeled Earthquake Catalogs Referred to in the Text^a

Catalog Name	Loading Condition	Number Faults
TR0	Uniform shear stress increase	1×10^5
UPR	Uniform pressure increase	1×10^5
UPR-E	UPR with stress evolution	4×10^5
H1	Advancing step function	4×10^5
2DF	2-D flow geometry	4×10^5
E2D	Extended 2-D flow	4×10^5
GG51	Wells 1 and 5 injection	1.5×10^5
GG51-1	Only Well 1 injection	1.5×10^5
GG51-5	Only Well 5 injection	1.5×10^5
GG52	10% Wells 1 and 5 injection	1.5×10^5
GG52-1	Only 10% Well 1 injection	1.5×10^5
GG52-5	Only Well 5 injection	1.5×10^5

^aTR0 = Tectonic Reference, UPR = Uniform Pressure Rise, UPR-E = Uniform Pressure Rise-Extended, 2DF = 2-D fault, E2D = extended 2-D flow, GG5*i* = Guy-Greenbrier scenario *i*, GG5*i*-*j* = Guy-Greenbrier scenario *i* with only Well *j* injecting.

arrest and thus tend to grow larger. At high enough values, the rupture is energetic enough that its dimension becomes unbounded and its upper limit is that of the fault, L_0 [e.g., Ben-Zion *et al.*, 2003; Ampuero *et al.*, 2006].

Thus, a distribution of L^* (Figure 3d) arises due to a distribution of faults with different stress levels, $\bar{\tau}^*$, which in turn is related to the amount of tectonic loading, $\Delta\tau_{\text{fail}}^*$, that precedes earthquake nucleation. In our model, initial stress on a fault, $\tau_0^*(x^*)$, is assigned through random draws from the stress PDF and thus $\Delta\tau_{\text{fail}}^* = \tau_s^* - \max(\tau_0^*(x^*))$ is also a random variable. The shape of the distributions of $\Delta\tau_{\text{fail}}^*$, $\bar{\tau}^*$, and, ultimately, L^* and M_W , is then determined by the shape of the stress PDF, as parameterized by σ_τ^* . For a magnitude frequency distribution with $n = 0.25$, the b value decreases with decreasing σ_τ^* (Figures 3b and 3c) and eventually transitions to a characteristic earthquake distribution ($L^* = 1$ for all events). This replicates a result of Ampuero *et al.* [2006], who also used a 1-D fracture mechanics model of faults with heterogeneous stress, and who observed a transition from GR to characteristic earthquake behavior across a similar range of σ_τ^* . Ripperger *et al.* [2007] confirmed a similar transition in 2-D dynamic rupture simulations for σ_τ^* in the range 0.1 to 0.4.

Because of the way in which tectonic loading is approximated, the magnitude frequency properties of catalog TR0 are mostly insensitive to μ_τ^* , which is here set to -0.54 . Setting a different value changes the size of $\Delta\tau_{\text{fail}}^*$ but preserves the stress at failure, $\tau_0 + \Delta\tau_{\text{fail}}^*$, and hence the GR scaling. An exception is when μ_τ^* approaches 1, in which case the effects of distribution truncation become significant and the magnitude frequency distribution departs from linearity.

3.4. A Stress Model for Tectonic Earthquakes on 1-D Faults

In the remainder of this paper, we assume that tectonic 1-D faults are characterized by a stress model with $n = 0.25$ and $\sigma_\tau^* = 0.225$. This produces a power law distribution of M_W and L^* , which we assume is a feature of earthquake distributions on 1-D faults. The distribution of M_W is characterized by a b value denoted b_{TR0} . The selection of $\sigma_\tau^* = 0.225$ results in $b_{\text{TR0}} = 1.15$, although the extent to which b value observations on 2-D faults should be used to constrain that a 1-D model is unclear. Nevertheless, we shall assume that deviations away from b_{TR0} in modeled 1-D induced earthquake catalogs are reflective of physical processes that may also operate on 2-D faults.

Physically, this model for heterogeneous stress represents the average conditions on a fault across all stages of the seismic cycle. It is used in the construction of catalog TR0, which comprises an ensemble of 10^5 faults. This and other simulated catalogs referred to in the text are summarized in Table 4.

4. Magnitude Frequency Properties of Modeled Induced Earthquakes

In this section, we model catalogs of induced earthquakes and investigate the evolution of their spatiotemporal and magnitude frequency distributions. The individual faults in each ensemble have the same friction parameters as catalog TR0. The initial stress on these faults is constructed using the same stress model as

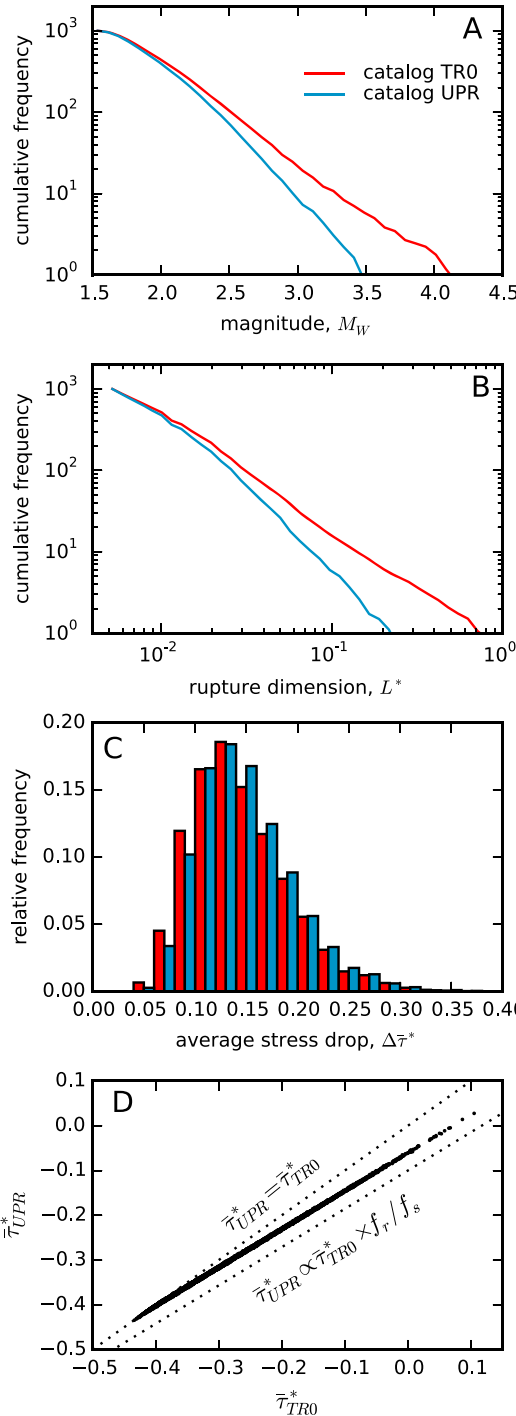


Figure 4. Magnitude frequency comparison between catalogs TR0 (red) and UPR (blue). (a) Magnitude frequency distribution. (b) Cumulative distribution of rupture lengths, L^* . (c) Histogram distribution of average stress drop, $\Delta\bar{\tau}^*$, in each catalog. (d) Average potential stress drop for comparable earthquakes in TR0, $\bar{\tau}_{TR0}^*$, and UPR, $\bar{\tau}_{UPR}^*$. Ruptures from two different catalogs are comparable if (i) they have the same initial stress profile, $\tau_0^*(x^*)$, and (ii) the same hypocenter location, x_h^* .

catalog TR0, i.e., $n = 0.25$ and $\sigma_\tau^* = 0.225$. For these faults, earthquakes are triggered by static strength reduction due to pressure rise on the fault.

4.1. Uniform Pressure Rise

We first consider a simple case of injection in which fluid pressure is constant across a fault and rises at a constant rate over time. In this hypothetical scenario, there are no pressure gradients, which we expect to exist in a realistic injection scenario. Nevertheless, this example illustrates several important concepts relevant to cases of more complex pressure loading. Catalog UPR (Uniform Pressure Rise) comprises 10^5 faults, uses identical stress realizations to TR0, and, because pressure loading is constant on the fault just as stress loading was constant for TR0, the modeled earthquake hypocenters are in the same locations. Therefore, in comparing UPR and TR0, the single point of difference is τ^* at the time of rupture, which for UPR is (from Table 3, equation (12))

$$\bar{\tau}^* = \bar{\tau}_0^* + \Delta P_{fail}^*, \quad \Delta P_{fail}^* = \frac{f_r}{f_s} (\tau_s^* - \max(\tau_0(x^*))), \quad (18)$$

where ΔP_{fail}^* is the pressure change causing failure. Note, for UPR, it is the pressure component of τ^* that changes, in contrast to the stress component that is modified for TR0 ruptures.

Figures 4a and 4b compare the magnitude frequency distribution and underlying rupture length, L^* , distributions for catalogs UPR and TR0. A shift to smaller magnitudes (increased b value) is evident and this appears to be related to a similar shift in L^* . The decreased magnitudes in Figure 4a cannot be accounted for by smaller stress drops (Figure 4c, in fact there is a slight shift to higher stress drops for UPR associated with the distribution shift to smaller L^* , cf. Figure 3f). The b value computed for UPR is 1.53, higher than b_{TR0} .

In this case, it is the shift to smaller L^* that is responsible for the b value increase. Comparing equations (17) and (18), we see that the potential stress drop, $\bar{\tau}^*$, is smaller for an event in UPR than for the same event in TR0 (see also Figure 4d). Effectively, stress on the fault is lower and, as a less energetic fault produces smaller ruptures (Figure 3e), there is a corresponding decrease in L^* . In turn, the discrepancy in $\bar{\tau}^*$ between TR0 and UPR can be traced back to the different rates at which static, τ_s^* , and residual strength, τ_r^* , drop as pressure is increasing.

So a b value increase is modeled for events triggered by uniform pressure rise on 1-D faults: is this

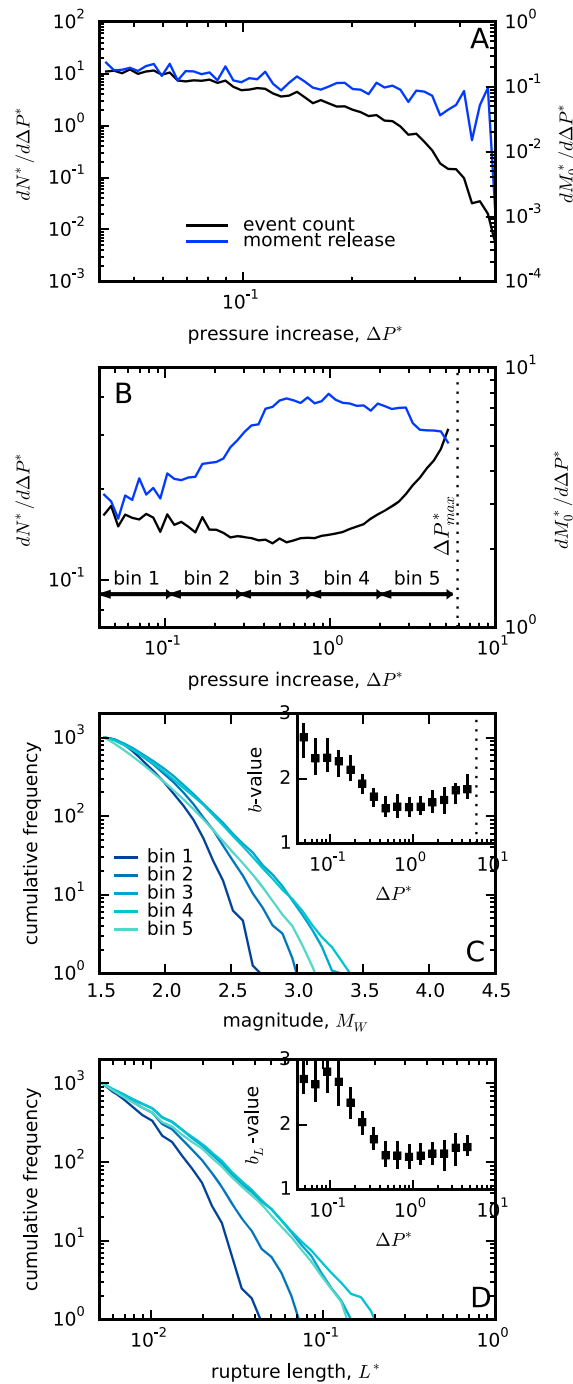


Figure 5. Summary of UPR and UPR-E catalogs. (a) Seismicity (black) and moment release (blue) per unit pressure rise for catalog UPR. The moment release profile oscillates at high ΔP^* because events are large but infrequent. Because pressure rises at a constant rate in this scenario, we use ΔP^* as a proxy for time, t^* . (b) Seismicity and moment release per unit pressure rise for catalog UPR-E. The theoretical maximum pressure, ΔP_{max}^* , where pressure exceeds normal stress, is indicated by a dotted line. (c) Magnitude frequency distributions for events in each of the five bins in Figure 5b. The evolving b value with error estimate is shown in the inset. (d) Rupture length distribution for the same bins as Figure 5c. Evolving b_L , computed by equation (5), with error estimate is shown in the inset.

result likely to apply for ruptures on 2-D faults? The underlying mechanism is a reduction in the potential stress drop at the time that earthquakes are triggered, and this in turn reflects the different rates at which τ_s^* and τ_r^* are decreasing. This mechanism is independent of the dimensionality of the problem and so might reasonably be expected to occur for 2-D fault ruptures.

4.1.1. Temporal Variation of the Magnitude Frequency Distribution

For catalog UPR, ΔP^* increases at a constant rate and is therefore a proxy for time. Thus, in Figure 5a seismicity and moment release “rates” are defined and plotted with respect to ΔP^* . The seismicity rate attains a maximum early on and then declines with time (i.e., ΔP_{fail}^*), which reflects a decreasing likelihood that a given stress realization is initialized satisfying $\max(\tau_0(x^*)) < \tau_s^* - f_s/f_r \Delta P_{\text{fail}}^*$ (a randomly distributed variable, see equation (18)). The moment release rate also decreases with time, although less rapidly than the seismicity rate. The diminished event rate is offset partly by relatively more energetic events as $\bar{\tau}^*$ increases (promoting larger L^* ; see Figure 3e).

In practice, we do not expect the seismicity rate to drop to zero with continuing pressure increase. Rather, we expect the rate of earthquakes to be steady or increase as sections of the fault that had previously ruptured fail once again with ongoing strength reduction. A limitation of our model is that it does not deterministically model stress redistribution associated with rupture; hence, we only consider one earthquake per fault realization. However, we can use an ensemble approach to approximate the evolving fault stress and therefore consider ongoing seismicity.

Catalog UPR comprises an ensemble of faults with initial stress, τ_0^* , constructed from a stress model that fixes n , σ_τ^* , and μ_τ^* . The extended catalog UPR-E, comprises a weighted ensemble of subcatalogs, each itself made up from an ensemble of faults. Each subcatalog comprises faults with realizations of $\tau_0^*(x^*)$ drawn from a stress model with different μ_τ^* and σ_τ^* that are monotonic linearly decreasing functions of ΔP^* (see Table 3, equations (15) and (16)). The smaller value for μ_τ^* means that fault realizations for that catalog have lower average stress; physically, this represents the state of the fault at later time when it is assumed that prior seismicity has reduced shear stress. Pressure evolution, ΔP^* , is the same for all faults and all subcatalogs. To

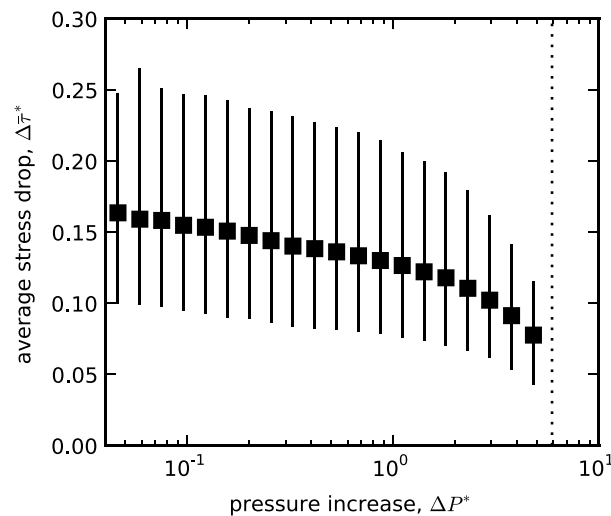


Figure 6. Evolving average stress drop for UPR-E catalog. The marker indicates the mean value and the bar indicates the interval enclosing 5 to 95% of values.

value is high. Over time, τ^* and moment release rate increase—events become more energetic—and as a result the b value declines. This is analogous to b value decrease on a fault as it nears the end of its seismic cycle [Smith, 1981]. Indeed, the magnitude frequency curves in Figure 5c replicate a similar evolution in the models of Ben-Zion *et al.* [2003] (cf. their Figure 7a) who analyzed how earthquake distributions evolved in the lead up to a system-wide rupture.

In the second phase, moment release rate and the rupture length, L^* , distribution (as parameterized by b_l , see equation (5) and Figure 5d, inset) are quasi-constant. Fault stress declines with increasing ΔP^* and as a result the average stress drop, $\Delta \bar{\tau}^*$, gets smaller (Figure 6). The effect is minor, but there is a small increase in the b value when magnitudes are computed with the $\Delta \bar{\tau}^*$ term. Correspondence between a high b value and low stress drop was suggested by Goertz-Allmann *et al.* [2011] in analyzing earthquakes triggered by high-pressure injection at the Basel EGS site. They showed relatively smaller $\Delta \bar{\tau}^*$ nearer to the injection well where pressure is higher. Once again, this mechanism for an increase in b value is linked to changes in stress on the fault and thus likely independent of the problem dimensionality (1-D versus 2-D faults). The seismicity rate increases during the second phase in compensation of the reduced stress drop per event (recall, our model of stress evolution requires that cumulative stress drop of all events keeps pace with total stress decline on the fault).

4.2. Nonuniform Pressure Rise

Having considered a hypothetical scenario of uniform pressure increase, we now consider more complex plume shapes produced under a variety of injection conditions. The catalogs simulated here inherit the statistical stress model ($n = 0.25$, $\sigma_\tau^* = 0.225$) and friction parameterization of catalogs TR0, UPR, and UPR-E. The parameters specifying a particular pressure-loading condition are flow scenario (2-D, extended 2-D, advancing front), fault permeability, and injection pressure. The shear stress level on the fault, parameterized by μ_τ^* in the stress PDF, is also varied. As in part one, we use the nondimensional ratio between injection pressure and fault criticality, $C_r = \Delta P_{inj}^*/(1 - \mu_\tau^*)$, to illustrate the range of seismicity behavior. This measure quantifies the relative size of changes in fault strength due to overpressure against natural variation in heterogeneous fault stress.

Spatiotemporal evolution of fault strength, τ_s^* and τ_r^* , is captured directly through their dependence on $\Delta P^*(x^*, t^*)$. However, as shown in the previous section, spatiotemporal evolution of fault stress is also important to consider, particularly for long periods of injection. Evolving fault stress is captured in the same manner as for catalog UPR-E, i.e., by considering an ensemble of subcatalogs with different values for μ_τ^* . The difference is that, since ΔP^* is spatially variable in these scenarios, for a given subcatalog, so too must μ_τ^* . Essentially, we assume that induced earthquakes reduce stress on a fault and that, at any given time, the average stress reduction is reflective of the pressure plume triggering those earthquakes. Again, in this ensemble sense, we

construct UPR-E, we compute weights for the individual events such that the sum of the stress drops, $\Delta \bar{\tau}^*$, of all events in a spatiotemporal increment matches the prescribed stress change on the fault in the same increment. Catalog UPR-E comprises 200 subcatalogs, which each contain 5000 fault realizations, and we now consider uniform pressure rise approaching the limit of tensile failure, i.e., $\Delta P^* \rightarrow \Delta P_{max}^*$.

Evolution of seismicity in UPR-E is divided into two phases. In the first phase, for $\Delta P^* < 0.5$, we observe quasi-constant seismicity rate, increasing moment release rate (Figure 5b), and decreasing b values from 1.8 to 1.2 (Figure 5c, inset). Physically, this represents the triggering of earthquakes on a fault in a subcritical failure state. Initially, potential stress drop, τ^* , is small (Figure 5d) because ΔP^* is low; thus, ruptures are small and b

do not explicitly represent stress signatures from prior events (stress drop inside a rupture and increase at the tips) as these are assumed to be captured, in an average sense, by the heterogeneous stress model.

4.2.1. Injection Onto a Fault

We contrast two scenarios of on-fault injection. In the first, pressure evolution is a prescribed Heaviside step function that advances away from the well according to a diffusion-like relationship, i.e., $r_f^* = \sqrt{t^*}$, where r_f^* is the distance between the front and the injection well. This scenario approximates the effects of seismicity coadvancing with a front of high permeability resulting from the induced shear slip [McClure and Horne, 2011; Gischig and Wiemer, 2013; Dempsey et al., 2015]. The catalog of seismicity associated with this scenario is denoted H1 (with $\Delta P_{inj}^* = 0.74$, $\mu_\tau^* = -0.54$) and its features are illustrated in Figure 7 (left column). In the second scenario, permeability is assumed constant and pressure evolves according to fixed-pressure injection in a 2-D geometry with constant pressure boundaries. The catalog of seismicity simulated for this scenario is denoted 2DF, it has the same ΔP_{inj}^* and μ_τ^* , and is summarized in Figure 7 (right column).

In both H1 and 2DF scenarios, the amount of seismicity along the fault (quantified as the density of simulated hypocenters) follows approximately the spatial distribution of pressure buildup (Figures 7a and 7b). This is a built-in feature of the model that arises from the definition of catalog event weights (see first paper for a discussion of catalog weighting). In the case of H1, the seismicity concentrates exclusively at the advancing front. For 2DF, the amount of seismicity decreases with distance from the well in accordance with a decaying pressure profile, and occurs farther from the well over time (as in H1). However, in 2DF, because pressure on the fault rises over time, so too are earthquakes continuously triggered across the fault (as opposed to a concentrated front region for H1).

The rate of earthquakes also differs between the two scenarios. For H1, the simulated seismicity rate, \dot{N}^* , declines as $1/\sqrt{t^*}$ (Figure 7c) in accordance with the rate of the advancing front. However, this is for a 1-D fault. An approximation of \dot{N}^* for a 2-D fault is obtained by applying a linearly increasing weight to events with hypocenters further from the well—this represents summing seismicity over concentric circles of increasingly larger area. Constructed this way, \dot{N}^* is constant with time, i.e., even though the advancing front slows with time, it carves out a larger area of the fault, and the two balance for a constant rate. For 2DF, the 1-D and 2-D seismicity rates increase slowly over time as earthquakes are triggered across a larger zone. For $t^* > 2 \times 10^{-4}$, seismicity rate declines; this reflects stabilization of pressure in the model due to equilibration with the pressure boundary condition and may not accurately reflect real cases of induced seismicity.

The magnitude frequency distribution for both scenarios (Figures 7e and 7f) shows a departure from the linearity seen previously. In the case of H1, the distribution is not consistent with past cases of induced seismicity and may derive its unconventional shape from the approximation of ΔP^* as a step function. The distribution for 2DF is more linear, with a b value of ~ 2 . There is also a deficit of large-magnitude events, which is a feature of some cases of induced seismicity [e.g., Dorbath et al., 2009; Huang and Beroza, 2015] and has been attributed to the finite dimension of a pressure plume [Shapiro et al., 2011]. Clearly, for the 2DF scenario, the pressure plume has a finite dimension and we can test directly whether this is responsible for the convexity in Figure 7f. To do this, we perform all rupture calculations again, this time under conditions of constant pressure increase (hypocenter locations are preserved). The magnitude frequency distribution for the resulting events is shown as a dashed line in Figure 7f and closely resembles a GR model with $b \sim 1$. For scenario 2DF then, we conclude that a finite plume dimension introduces convexity in the magnitude frequency distribution.

The presence of a plume shape effect on convexity of the magnitude frequency distribution was investigated for a range of injection pressures, ΔP_{inj}^* and fault failure proximity, as parameterized by μ_τ^* (Figure 8a). The relative effect of these two parameters on fault stability is captured by the criticality/pressurization ration, C_r (see Table 3, equation (12)). The amount of introduced convexity, ΔM_{max} , is quantified as the difference between largest magnitude events for a simulated catalog and the equivalent catalog with the shape effect removed. A bootstrap sampling algorithm is used to estimate an interval for ΔM_{max} , similar to that used to estimate a GR b value (Appendix A). For the 2-D flow geometry, we tend to see a stronger plume shape effect for high C_r . Physically, this corresponds to greater control on the dimension of rupture by the pressure component, ΔP^* , of potential stress drop, τ^* (compared with the stress component, τ_0^* , see Table 3, equation (12)). Such high values for C_r are more likely to occur during well stimulations, such as during creation of an EGS or hydraulic fracturing, and it is notable that observations of convexity in the magnitude frequency distribution have been associated with these types of injection [e.g., Dorbath et al., 2009; Friberg et al., 2014]. Convexity due to the plume shape effect also occurs in simulations with the advancing front (Figure 7e), although the magnitude

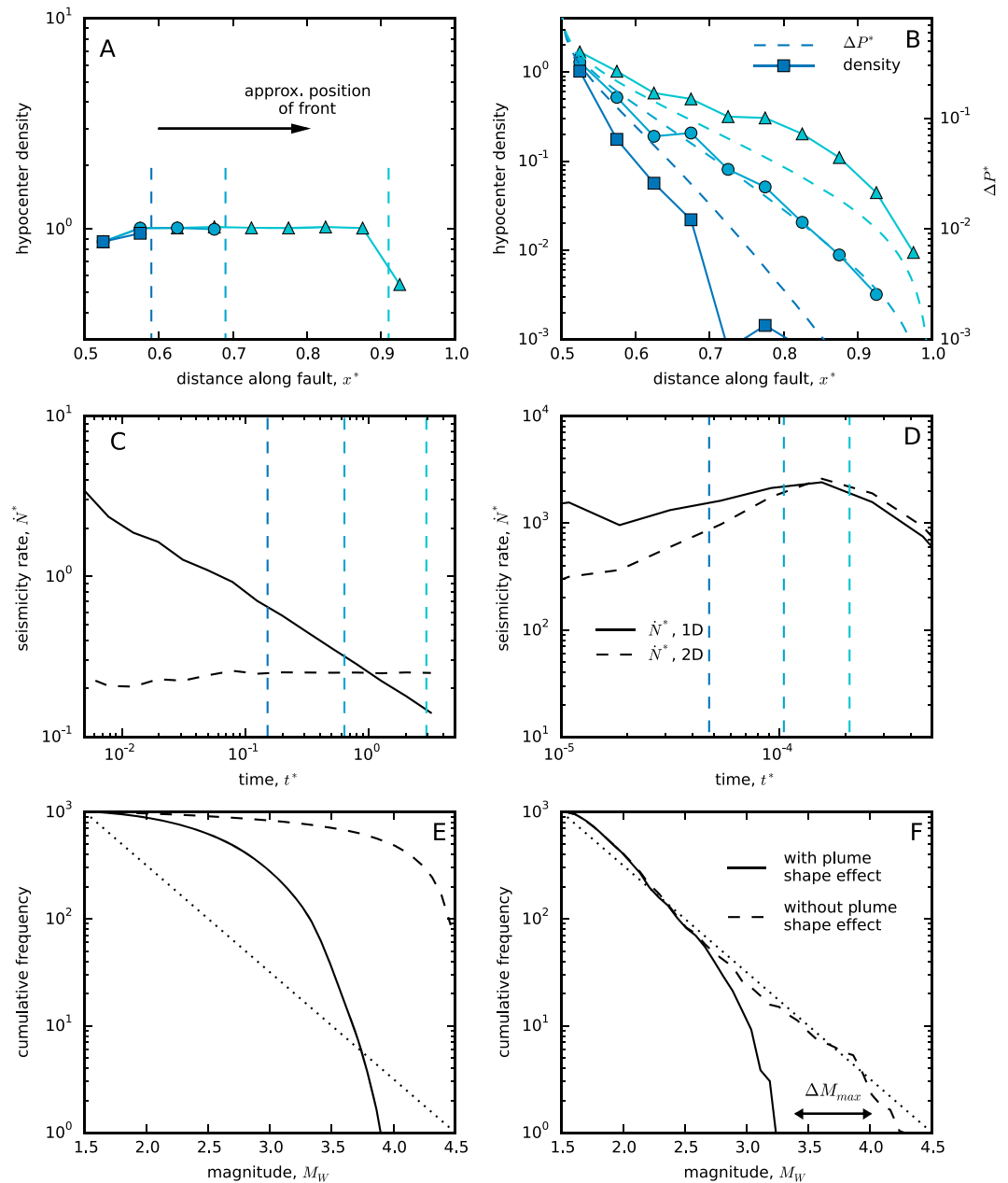


Figure 7. Summary and comparison of scenarios (left column) H1 and (right column) 2DF. (a, b) Density of simulated earthquake hypocenters at three different times during injection. For comparison, the shape of the pressure distribution at each of the three times is indicated by the corresponding colored dashed line. (c, d) Modeled seismicity rate, \dot{N}^* , versus time (solid line) and the equivalent seismicity rate for a 2-D flow system (dashed; linear increase of event weighting for hypocenters further from the well). This weighting scheme introduces minor numerical artifacts at early time when weights are small and there are not many simulated events—these appear as fluctuations in the profile. (e,f) Magnitude frequency distributions for events simulated with (solid line) and without (dashed) pressure plume shape effects. The pressure plume shape effect is approximately removed by replacing nonuniform $\Delta P(x^*, t_h^*)$ with constant $\Delta P(x_h^*, t_h^*)$ in the definition of τ^* in the calculation of rupture length (see Table 3, equation (7)). The change in maximum earthquake magnitude, ΔM_{max} , is indicated.

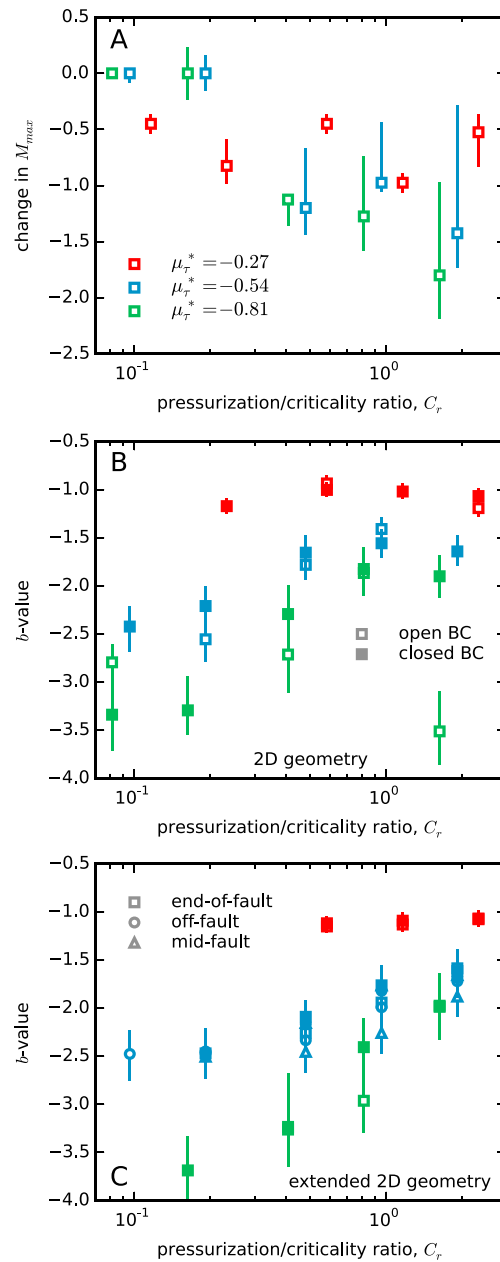


Figure 8. (a) ΔM_{max} due to plume shape effect (see Figure 7f for definition) across a range of injection pressures, ΔP_{inj}^* and initial fault stress, μ_{τ}^* . The pressurization/criticality ratio is defined as $C_r = \Delta P_{inj}^* / (1 - \mu_{\tau}^*)$. Marker and vertical bar indicate the mean and interval containing 90% of ΔM_{max} values for 1000 bootstrap samples of the simulated catalog. Simulations are for 2-D flow geometry with open boundary conditions. (b) Simulated b values obtained from fitting a GR model for a range of ΔP_{inj}^* and μ_{τ}^* . Simulations are for 2-D flow geometry. Only simulations in which the mean curvature of the magnitude frequency distribution, C_v , is less than 0.4 are shown. (c) As for Figure 8b but for simulations of the extended 2-D flow geometry. In all subplots, symbol color denotes the value of μ_{τ}^* , open and closed symbols indicate simulations with open and closed boundary conditions, respectively, and symbol type indicates injection well position for the extended 2-D flow geometry.

frequency distributions depart quite strongly in shape from linear and nonlinear GR models. Convexity is not observed in simulations that employ a closed boundary condition. This is because early events that exhibit the shape effect are masked by the later-time events, which do not (because pressure buildup is quite uniform). This situation could possibly arise for reactivated faults inside a closed reservoir. Nor do we observe convexity for the extended 2-D flow geometry, which approximates a wastewater injection scenario, although there are indications that such effects can be present in these sequences as well [Huang and Beroza, 2015].

Sensitivity of the GR b value is also of interest. Figure 8b plots b value for injection in a 2-D flow geometry and for a range of ΔP_{inj}^* , μ_{τ}^* and models with both open and closed boundaries. The b value is computed for the entire catalog and therefore averages over any variability in space or time. As some of the magnitude frequency distributions modeled here depart quite strongly from linearity, only b values for distributions reasonably approximated by a GR model are shown (see Appendix B for quantification of linearity). To first order, simulated b values reflect the average fault shear stress as parameterized by μ_{τ}^* . This directly effects the potential stress drop, τ^* , which describes the energy available for rupture and therefore provides a strong control on L^* (Figure 3). This feature of the model is consistent with microfracture experiments [Scholz, 1968] and tectonic observations [Schorlemmer et al., 2005] that infer a similar relationship between b value and level of shear stress. In our study, the relationship emerges from an energy-based description of the rupture process coupled to a model of fault stress heterogeneity.

The sensitivity of b value to shear stress has an interesting implication for situations in which injection reactivates multiple faults. Assuming that the regional stress field is approximately constant, faults of different orientation will have resolved on them different levels of shear stress. According to Figure 8b, the b value for seismicity specific to a fault would increase with increasing misorientation of the structure in the prevailing stress field.

4.2.2. Injection Away From A Fault

We now consider induced seismicity in an extended 2-D flow geometry, which approximates injection into a horizontal aquifer triggering earthquakes on a connected basement fault. This geometry is distinct from other configurations in that injection does not occur directly onto the fault. Thus, the fault is shielded from the highest pressures and steepest pressure gradients, which occur in the aquifer. For

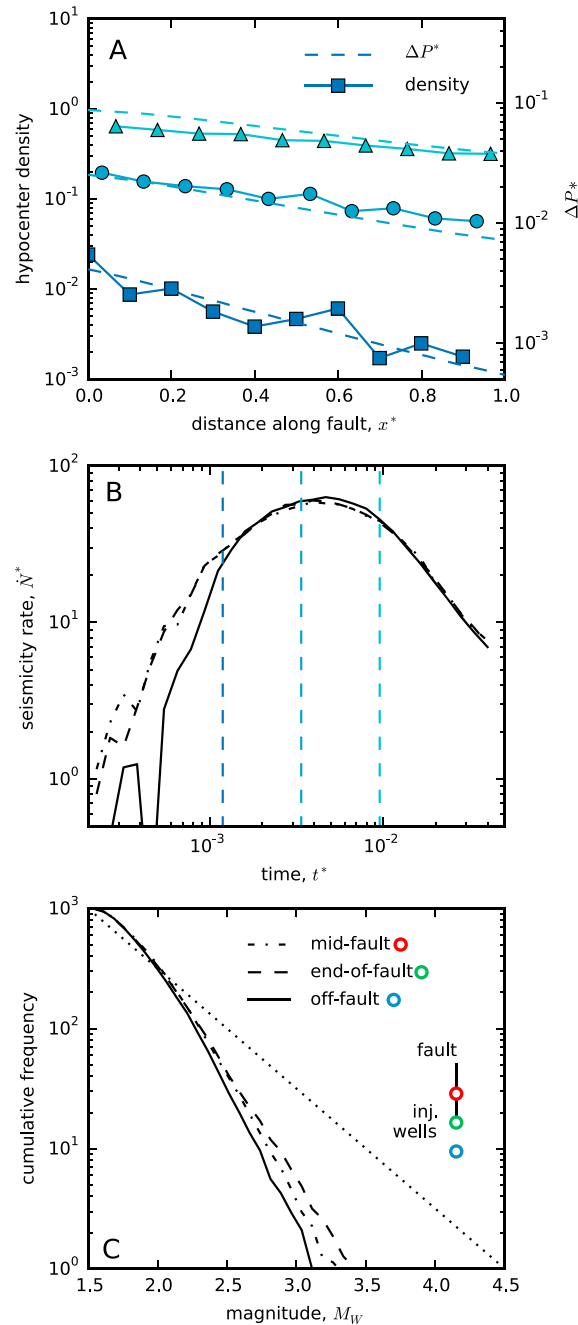


Figure 9. Summary of scenario E2D, injection in extended 2-D flow geometry with well in the off-fault position. (a) Density of simulated earthquake hypocenters at three different times during injection. For comparison, the shape of the pressure distribution at each of the three times is indicated by the corresponding colored dashed line. (b) Modeled seismicity rate, \dot{N}^* , versus time. Numerical artifacts at early time are due to the small number of catalog events. Dashed and dash-dotted profiles indicate the seismicity rate for end-of-fault and midfault injection well positions. (c) Magnitude frequency distributions for catalog E2D and comparison with alternative injection well positions. Inset shows the locations of the three well positions relative to the fault.

these simulations, aquifer permeability is set to 10^{-14} m² and porosity to 0.1, typical of wastewater disposal formations. Fault permeability is set to 10^{-14} m². Catalog E2D is simulated for injection in the off-fault position, although results for other positions are shown in Figure 9. Pressure rise at a depth $L_0/4$ in the basement is used in computing triggered seismicity. For the reference scales used here ($L_0 = 4$ km and $M_{W,0} = 4.5$), this would correspond to a depth of 1 km below the aquifer-basement contact.

Figure 9a shows that, as for H1 and 2DF, the spatial distribution of seismicity follows contours of pressure buildup. The modeled seismicity rate increases approximately quadratically with time for a period but eventually reaches a maximum and starts to decline as pressure in the system comes to equilibrium (Figure 9b). Simulated events are characterized by a magnitude frequency distribution with GR b value higher than the simulated tectonic value. The increase in b value is caused by the different rates of reduction of static and residual strength when effective normal stress is lowered, as discussed in section 4.1. Both the modeled seismicity rate and magnitude frequency distribution are similar for the three injection well positions. As for the 2-D flow geometry, catalog b values show a strong dependence on initial shear stress (Figure 9c).

It is worth noting that several cases of induced seismicity associated with wastewater injection suggest a reduction of b value below the tectonic average during the injection phase [Lei et al., 2008, 2013; Huang and Beroza, 2015; Goebel et al., 2016]. This behavior is not accounted for within our model and it is not clear whether this is due to parameter selection or shortcomings in either the stochastic approach or 2-D approximation.

5. Model Application to the Guy-Greenbrier Sequence (2010–2011)

In this final section, we discuss an application of our model to a sequence of earthquakes in Arkansas in 2010–2011 that were likely to have been triggered by wastewater disposal at two nearby injection wells. The Guy-Greenbrier sequence, named for the two towns between which the earthquakes occurred, is described in Horton [2012] and much of the discussion of the

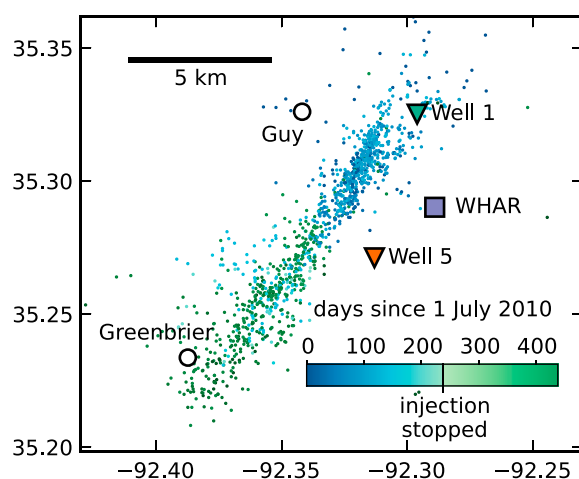


Figure 10. ANSS catalog locations and times in the context of the nearby towns of Guy and Greenbrier. The locations of two injection wells, referred to as Well 1 and Well 5 in Horton [2012] and a single broadband seismic station, WHAR, used to determine event magnitudes in Huang and Beroza [2015] are also shown.

and Zoback, 1991]. Seismicity tended to migrate in a southwest direction along the Guy-Greenbrier Fault (Figure 10), away from the largest volume injector, Well 1 (Figure 11a). A single permanent broadband station of the Arkansas seismic network, WHAR, is located near the Guy-Greenbrier Fault (Figure 10). Huang and Beroza [2015] applied a template matching technique to continuous records from this station and detected an average of 160 earthquakes per hour when the sequence was at its most productive (during the same period, the ANSS catalog registered approximately seven earthquakes per day). They used an Akaike information criterion to show that the evolving magnitude frequency distribution of the WHAR catalog exhibited a nonlinear GR distribution during injection, characterized by low b values (~ 0.8) and convexity at the large-magnitude end. The magnitude frequency distribution returned to a GR model with $b=1$ once injection was halted.

Two wastewater injection wells are thought to be responsible for triggering the Guy-Greenbrier earthquakes. Well 1 started operating at the beginning of July 2010 and injected a total volume of $3.9 \times 10^5 \text{ m}^3$, while Well 5 started in mid-August 2010 and injected $0.7 \times 10^5 \text{ m}^3$. Injection at both wells was halted following an M 4.7 earthquake on 27 February 2011 [Horton, 2012]. Both wells inject into the Ozark Aquifer, a $\sim 1 \text{ km}$ thick geohydrologic unit that is dominantly dolostone (low intrinsic porosity, $\sim 4\text{--}6\%$), with some limestone and sandstone formations [Horton, 2012]. Well 5 injects deeper in the Ozark and has a larger open-hole interval, whereas Well 1 injects over a 30 m interval at the top of the Ozark [Horton, 2012] as well as into the overlying Springfield Aquifer.

We construct a reservoir model of injection at Wells 1 and 5 for the time period July 2010 to October 2011 and use the modeled pressure buildup on the Guy-Greenbrier Fault to construct a model of the seismicity. Because the model is a stochastic representation of the earthquake sequence, our goal is to capture only its average features. In particular, we focus on (i) the onset time of seismicity on the fault, (ii) the migration rate of seismicity along the fault, and (iii) the decay in seismicity after injection was halted.

5.1. Model Setup and Calibration

Pressure evolution in the Guy-Greenbrier system is computed using a variation of the extended 2-D flow geometry with key parameters summarized in Table 5. Aquifer thickness is set to 1 km and assigned a homogeneous porosity (4%) [Horton, 2012] and permeability. Well 5 penetrates the full vertical extent of the aquifer whereas Well 1 only penetrates the top 30 m and also injects into an overlying formation. The flow simulator FEHM is once more used to perform mass balance calculations under the assumption of isothermal flow. A reference temperature of 30°C is used to calculate viscosity and density. Both porosity and permeability are assumed constant. Grid blocks have lateral dimensions of $250 \times 250 \text{ m}$ in the vicinity of the injection wells and fault, and are larger nearer the closed flow model boundaries (5 km from the fault well configuration). The basement is vertically discretized using 500 m thick layers, while the aquifer is divided into a 30 m thick top layer and 970 m thick bottom layer. Improved representation of vertical flows in the aquifer would be

seismicity and hydrological system is summarized from that study. In constraining the model, we make use of two earthquake catalogs reported in Huang and Beroza [2015], as well as monthly injection rates for two disposal wells in the area (designated 1 and 5 after Horton [2012]).

For mapping the spatiotemporal evolution of seismicity in the Guy-Greenbrier area we use locations from the ANSS (Advanced National Seismic System) catalog, which registered 1317 earthquakes in the Guy-Greenbrier area between July 2010 and October 2011, the time period covered by the model. These events define a linear structure—the Guy-Greenbrier Fault—striking $\sim N30^\circ E$ [Horton, 2012] and therefore well oriented for strike-slip failure with respect to the stress field of the U.S. midcontinent [Zoback

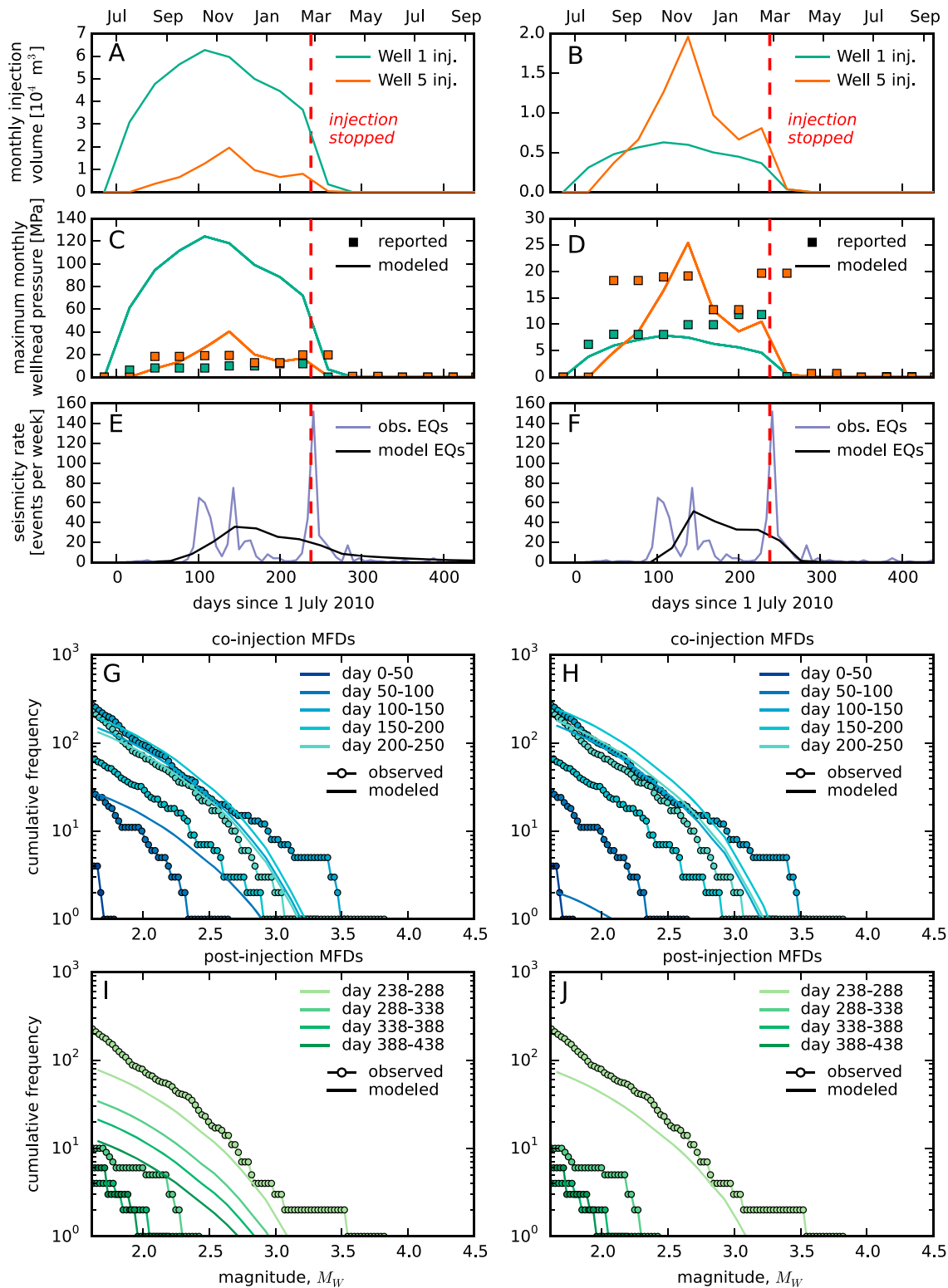


Figure 11. Observed and modeled evolution of injection, seismicity, and magnitude frequency distributions at Guy-Greenbrier for two scenarios (left = GGS1, right = GGS2). (a, b) Modeled monthly injection rates at Wells 1 (green) and 5 (orange). The red dashed line indicates the date at which injection was halted. (c, d) Modeled wellhead pressure at Wells 1 and 5 in response to the injection [Peaceman calculation Peaceman, 1983]. Square symbols indicate maximum reported wellhead pressure for that month. (e, f) Observed (purple) and modeled seismicity rate (black). (g, h) Observed (symbols) and modeled magnitude frequency distributions for 50 day bins from the beginning of injection (day 0) and (i, j) for 50 day bins from the end of injection (day 238).

Table 5. Parameters Used in Guy-Greenbrier Reservoir Model

Parameter	Value
Aquifer thickness	1 km
Fault width	10 m
Fault length	11 km
Fault height	4 km
Reference temperature	30°C
Fluid density	$1.0 \times 10^3 \text{ kg m}^{-3}$
Fluid viscosity	$8.0 \times 10^{-4} \text{ Pa s}$
Aquifer permeability	$1.0 \times 10^{-13} \text{ m}^2$
Fault permeability	$5.0 \times 10^{-12} \text{ m}^2$
Aquifer porosity (GGS1)	4.0%
Aquifer porosity (GGS2)	0.8%

obtained for higher grid resolution; however, the present model is sufficient for a first-order investigation of the Guy-Greenbrier seismicity.

Due to uncertainty about how much mass injected into Well 1 ends up in the Ozark Aquifer (it also injects into the Springfield Aquifer), we consider two bounding scenarios, denoted GGS1 and GGS2, in which (1) 100% and (2) 10% of the reported mass is injected into the Ozark. For GGS2, a smaller porosity is used (0.8%). Reported monthly injection volumes, linearly interpolated, are used as mass source terms (Figures 11a and 11b). A Peaceman solution [Peaceman, 1983] is used to approximate simulated wellhead pressure from the pressure in

the gridblock into which injection occurs. The simulated wellhead pressure is compared against reported monthly maximum values in (Figures 11c and 11d). Maximum injection pressures are approximately twice as high at Well 5 than at Well 1. The Guy-Greenbrier Fault is modeled as an 11 km long, 4 km deep, 10 m thick, vertically oriented, permeable plane embedded in impermeable basement. Pressure evolution at a depth of 1 km is used as the loading condition, $\Delta P(x, t)$, in the earthquake simulation model. Friction (f_s, f_r) and stress model parameterization (n, σ_r^*) are the same for previous simulated catalogs in this paper. To avoid triggering earthquakes at extremely low pressures, we set the maximum shear stress to 0.015 MPa less than $\tau_{s,0}$, which is approximately 5 times the magnitude of tidal forces on the fault [e.g., Vidale *et al.*, 1998]. Catalogs simulated for both injection scenarios comprise rupture on 1.5×10^5 fault realizations with evolving fault stress according to the method described in section 4.2. For plotting purposes, the earthquake magnitude scale is calibrated with $M_{w,0} = 5.5$, which is consistent with seismological scaling relations for complete rupture of a fault 11 km long [Zoback and Gorelick, 2012]. Modeled faults are discretized into 4096 nodes, which sets a minimum modeled magnitude of 1.6. There are three unknown parameters for model calibration: aquifer permeability, fault permeability, and proximity of the fault to failure, μ_r^* .

As in previous sections, temporal evolution of the seismicity rate is approximated by the PDF of catalog event times. This describes relative changes in the seismicity rate during injection and postinjection periods but does not constrain the absolute number of events. To be consistent with the observed earthquake rate at Guy-Greenbrier, we scale the total number of simulated events to be equal to the number of $M > 1.6$ events in the ANSS catalog. Observed and modeled seismicity rates for the two scenarios are shown in Figures 11e and 11f.

The onset of significant seismicity occurs ~ 100 days after injection begins at Well 1. We find the onset timing of seismicity to be quite sensitive to aquifer permeability. This is intuitive because aquifer permeability controls the timescale for pressure diffusion from the injection wells to the fault. Aquifer permeability is also an important parameter for calculating wellhead pressure increase via the Peaceman solution. For both scenarios, we find that an aquifer permeability of 10^{-13} m^2 yields a reasonable match to both seismicity onset time and simulated wellhead pressures at Well 5 (Figures 11c and 11d). For GGS1, the simulated wellhead pressure at Well 1 is significantly overestimated. This motivates the design of GGS2 with its reduced injection volume for Well 1 and, subsequently, an improved fit to the reported pressure data. Alternatively, pressure at the Well 1 would be lower if local permeability were higher, as might occur if the formation was hydraulically fractured. In this case, pressure evolution in the aquifer and simulated seismicity would resemble GGS1. However, the reduced injection volume required that we artificially lower porosity by a factor of 5 so as to enable large enough pressure buildup at the fault for earthquakes to be triggered. Physically, this corresponds to a lower average-connected porosity over the 1 km thick aquifer, which could occur if there are less permeable intermediate units. Alternatively, we cannot rule out a scenario in which the Ozark Aquifer is locally more permeable in the vicinity at Well 1, which would enable a greater volume to be injected here without exceeding observational constraints on pressure. Nevertheless, these two scenarios serve as a basis with which to explore induced seismicity on the Guy-Greenbrier Fault in general terms.

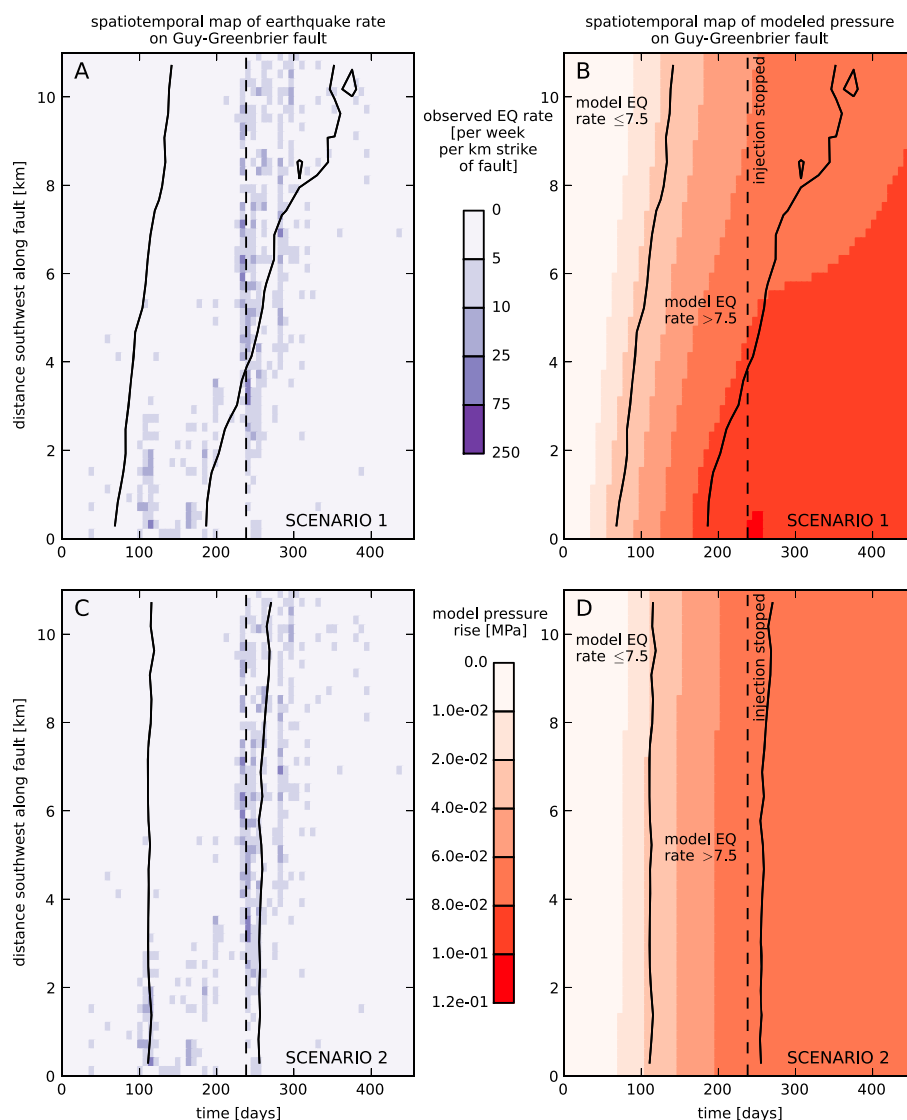


Figure 12. Summary of spatiotemporal evolution of earthquake activity and pressure plume at Guy-Greenbrier: data and two modeled scenarios (top = GGS1, bottom = GGS2). (a, c) Density map showing along-strike ANSS locations and timing of seismicity along the Guy-Greenbrier fault. The origin corresponds to the NE end of the fault (nearest to Well 1). (b, d) Modeled pressure evolution along the fault with time. The solid contours enclose the region where modeled earthquake rate density >7.5 events per week per kilometer along the strike of the fault.

Nine magnitude frequency distributions for 50 day bins covering both injection and postinjection periods are shown in Figures 11g–11j alongside modeled distributions for the same time periods. *Huang and Beroza [2015]* studied the evolving magnitude frequency distribution at Guy, Arkansas, and noted convexity at large magnitude and a reduction of b value during injection. Our model does not replicate either of these features for an extended 2-D flow geometry. However, we are able to approximate the slope of the observed magnitude frequency distribution by setting μ_t^* to -0.33 (see Figure 8c).

The final calibration target is the along-strike evolution of seismicity on the Guy-Greenbrier Fault. The spatiotemporal evolution of the seismicity rate, defined in terms of the number of events per week per kilometer along the strike of the fault, is shown in the activity maps in Figures 12a and 12c, which illustrate the overall shift in activity on the fault from the northeast to southwest. Overlaid on these maps are contours of the modeled seismicity rate for the two scenarios, enclosing an area in which the average modeled rate exceeded 7.5 events per week per kilometer along the strike of fault. For GGS1, where the larger pressure disturbance is created at Well 1, the rate at which seismicity migrates along the fault is qualitatively reflected in contours

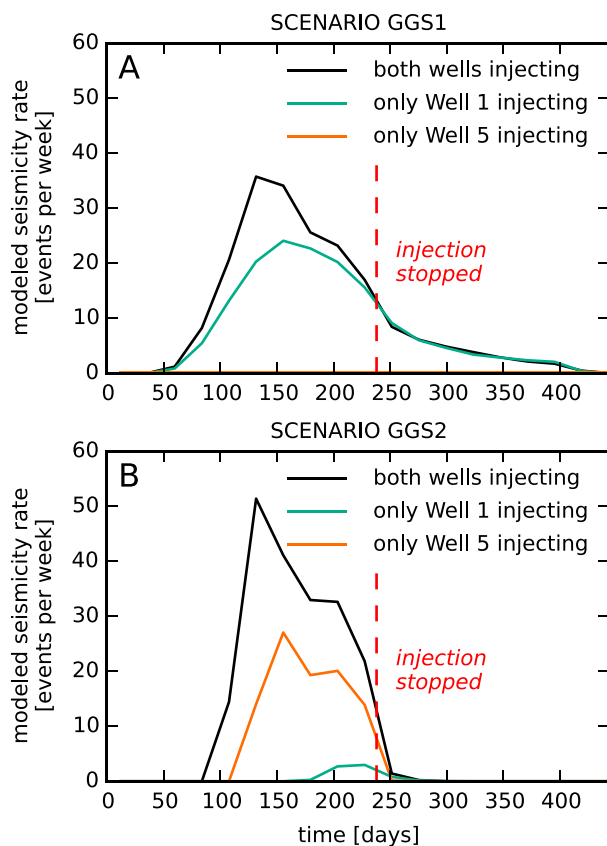


Figure 13. Modeled injection rates for alternative history seismicity simulations. (a) For GGS1, alternative catalogs GGS1-1—only Well 1 operating (green); and catalog GGS1-5—only Well 5 operating (orange; note, no seismicity was triggered in this case). Seismicity rate for catalog GGS, in which both Wells 1 and 5 are operating, is given by the black line. (b) As for Figure 13a but for scenario GGS2.

continues to rise on the fault. However, because the rate of pressure increase has slowed, the earthquake rate decreases. In the scenarios presented here, earthquakes are triggered at quite low fluid pressure. This is constrained by (i) observations of wellhead pressure, (2) aquifer thickness and porosity, and (3) the distance between injection wells and the fault. Modeled triggering pressures could be higher if further information were made available justifying a change in the conceptual model of the aquifer or other model parameters.

5.2. Hypothetical Injection Scenarios

One of the advantages of numerical modeling is the ability to consider “what-if” scenarios. For each of the simulated Guy-Greenbrier scenarios, we consider two hypothetical variations: injection that occurs only into Well 1 or only into Well 5. To aid the comparison, for each of hypothetical scenario, all other catalog properties are fixed, i.e., the injected volume at each well, flow, and fault stress properties, scaling coefficient for calibrating seismicity rate in Figures 11e and 11f. The alternate realities that result describe a different evolution of seismicity rate on the Guy-Greenbrier Fault (Figure 13). Table 6 compares the key features of these catalogs, denoted GGSi-j where i indicates scenario number and j which of the wells injects in the alternative scenario.

For GGS1, Figure 13a indicates that seismicity is dominated by high-volume injection into Well 1. No seismicity is predicted by the model for injection into Well 5 alone (pressure buildup on the fault is not large enough to exceed the 0.015 MPa threshold). For GGS2 (10% injection volume in Well 1), seismicity is instead dominated by Well 5 (Figure 13b) albeit with a poorer match to the spatiotemporal migration of seismicity (Figure 12).

Consideration of these hypothetical scenarios reveals an interesting nonlinearity in the model. Rates of induced seismicity for both GGS1 and GGS2 are not simple sums of their constituent hypothetical scenarios (GGSi-1 and GGSi-5), but rather the total seismicity is “more than the sum of its parts”. For prescribed injection

that tilt from the vertical. The degree of tilt is sensitive to the permeability of the fault, which for GGS1 is set to $5 \times 10^{-12} \text{ m}^2$ for an approximate match. The implication of a basement fault that is quite permeable is consistent with borehole observations [Barton *et al.*, 1995] which suggest that permeable fractures and faults are those with a favorable orientation for reactivation in the prevailing tectonic stress field. Llenos and Michael [2013] use an analytical diffusion model that assumes 3-D (spherical) flow [Shapiro *et al.*, 1997] to model the migration of seismicity along the Guy-Greenbrier Fault. Without an estimate of the elastic properties of the aquifer, we cannot compare the range of diffusivities that they obtain, 0.01 to $0.1 \text{ m}^2 \text{ s}^{-1}$, to the permeability estimates inverted by our model.

In contrast, modeled migration of seismicity is much less significant for GGS2 (Figure 12c). Instead, pressure buildup is more uniform along the fault (Figure 12b) as, in this scenario, Well 5 exerts the larger pressure influence.

Coevolution of fluid pressure on the fault for GGS1 and GGS2 is shown in Figures 12b and 12d alongside the corresponding seismic activity maps. High rates of earthquake activity occur when pressure on the fault is rising most rapidly. After injection is stopped, pressure con-

Table 6. Summary of Guy-Greenbrier Simulated Earthquake Catalogs^a

Catalog Name	GGSi	GGSi-1	GGSi-5	GGiS2	GGiS2-1	GGiS2-5
Operating wells	1(100%) & 5	1(100%)	5	1(10%) & 5	1(10%)	5
Volume injected [$\times 10^5$ m ³] (% of GGSi)	4.6	3.9 (85%)	0.7 (15%)	1.1	0.4 (37%)	0.7 (63%)
Peak seismicity [days since July 2010]	132	156	n/a	132	228	157
Number events $M_W \geq 1.6$ (% of GGSi)	743	578 (78%)	0 (0%)	743	26 (3.5%)	358 (48%)
Largest event	3.3	3.1	n/a	3.3	2.5	3.1

^aSee Table 4 for an explanation of the catalogs. Bracketed percentages for GGSi-j indicate amount of that quantity relative to scenario GGSi.

rate, the equations for mass flow in porous media are linear and therefore reservoir pressure in GGSi is the superposition of pressures in GGSi-1 and GGSi-5. However, the interaction of pressure buildup with a threshold for earthquake triggering (in this case, 0.015 MPa) introduces the nonlinearity. This feature of the model has a more practical implication, specifically that from a fault stability perspective; it is important to consider the combined effect of multiple injection wells in a region [Dempsey *et al.*, 2014]. Depending on the proximity and volume of concurrent injectors, amount of seismicity, timing of the peak, and the largest triggered event can vary (Table 6).

We note that our stochastic approach to modeling seismicity restricts our ability to comment on any specific reality. For instance, the relative seismicity rate curves in Figure 13 can be used as a probabilistic guide to the relative risk inherent in different injection strategies but, like all models, are weak to systemic flaws in model design, e.g., the existence of localized features (permeable fractures, impermeable barriers) that promote the pressure influence on the fault of one well relative to another.

6. Conclusion

Catalogs of induced earthquakes on 1-D faults are modeled through a fracture mechanics approximation of crack propagation physics, reservoir simulation of fluid pressure evolution, and a statistical model of fault shear stress (section 2; Figure 2). Heterogeneous shear stress is characterized by a fractal model with fractal exponent $n = 0.25$, and a Gumbel stress PDF with nondimensional standard deviation $\sigma_\tau^* = 0.225$ (section 3; Figure 3). The magnitude of simulated ruptures is expressed in terms of the rupture length, L^* , and the average stress drop, $\Delta\bar{\tau}^*$. When simulating a simplified tectonic loading condition, a magnitude frequency distribution that conforms to a Gutenberg-Richter model with a b value of 1.15 is obtained. Rupture size is shown to increase with increasing potential stress drop, τ^* (Figure 3e), which is the difference between shear stress and residual strength, i.e., a measure of available energy on the fault. The definition of τ^* includes contributions from both fault shear stress and fluid overpressure.

We investigate the change in magnitude frequency distribution (compared to the modeled tectonic case) under four scenarios of fault pressure evolution; they are as follows: (i) constant rate, uniform pressure increase, (ii) 2-D flow, approximating injection onto a fault at constant permeability, κ_f , (iii) a two-value, advancing step function, approximating fault injection when there is slip-induced enhancement of κ_f , and (iv) extended 2-D flow geometry, approximating injection into an aquifer overlying an impermeable basement hosting a permeable fault. Associated with these models of 1-D fault rupture, we draw the following conclusions that, owing to their underpinning by stress and strength evolution, are likely to be qualitatively valid for 2-D faults:

1. The simulated tectonic b value increases with increasing roughness in the stress profile, as parameterized by σ_τ^* (section 3.3, Figure 3c) (see also Ampuero *et al.* [2006] and Ripperger *et al.* [2007]). This is because greater roughness prevents propagating rupture fronts from jumping across negative stress drop regions and thus linking up positive stress drop sections into large events.
2. The simulated b value is higher for events triggered by pressure increase than for the same events triggered by stress increase (section 4.1, Figure 4). This is because fluid pressure increase causes the static strength to drop at a faster rate than the residual strength such that, when an earthquake is triggered, the average stress level on the fault (τ^*) is lower than the equivalent tectonic event by a factor f_r/f_s (the ratio of residual to static friction). For $f_r = 0.55$ and $f_s = 0.64$, the simulated b value increases from 1.15 for tectonic triggering to 1.53 for pressure triggering. Lower potential stress drop inhibits small ruptures from growing into large ones, because it is increasingly difficult for the rupture front to traverse wider and deeper regions of negative stress

- drop. The increased frequency of smaller ruptures is reflected in a b value increase (section 4.1.1, Figure 5). A similar relationship between stress and b value is observed in microfracturing experiments [Scholz, 1968], and this appears to extend to tectonic earthquakes worldwide [Schorlemmer *et al.*, 2005].
3. When injection and earthquake triggering begin, the simulated b value is initially high but then declines over time. As in the previous point, this is underpinned by the dependence of b value on τ^* , which tends to increase over time due to the effects of pressure rise on the fault (and the associated reduction of residual strength). The b value reduction with pressure rise is analogous to b value reduction inferred [Smith, 1981] and modeled [Ben-Zion *et al.*, 2003] on faults approaching the end of their seismic cycle. However, for natural seismicity it is an increase in shear stress rather than the decrease in residual strength that is responsible for the b value shift.
 4. Eventually, ongoing pressure rise reverses the b value decrease and it starts to climb again (Figure 5). This is a second-order effect in our simulations but may be stronger under parameter configurations not considered here. The effect arises because, as pressure increases and effective normal stress declines, the average stress drop of the simulated ruptures, $\Delta\tau^*$, becomes smaller. As $\Delta\tau^*$ is used in the calculation of event magnitude, this ultimately translates to smaller events and a higher b value. This result is consistent with observations of low stress drop near high-pressure well stimulations [Goertz-Allmann *et al.*, 2011].
 5. For faults with low initial stress, the simulated b value is higher (Figures 8b and 8c). Again, this reflects the increased difficulty of faults with low stress (τ^*) to grow small ruptures into larger ones. This implies that, for a collection of differently oriented faults in the same regional stress regime, the greater the misorientation of each fault (and hence the lower the resolved stress) the higher the expected b value for seismicity triggered on that fault.
 6. Under some conditions, it is possible for convexity to appear in the magnitude frequency distribution (Figure 8a). Physically, this represents a deficit of large-magnitude events relative to the number of small-magnitude events that have occurred. The effect arises because, energetically, conditions are more favorable for rupture inside the pressure plume than outside. This then imposes a preferred length scale for rupture—as well as a corresponding M_{\max} —and discourages events that try to grow larger than this limit. In our simulations, the effect only occurred for injection directly onto a fault and was more pronounced for high injection pressure. This is consistent with observations of such convexity in an EGS context [e.g., Dorbath *et al.*, 2009; Shapiro *et al.*, 2011] but does not account for recent observations of convexity associated with wastewater disposal [Huang and Beroza, 2015]. It has recently been suggested [McGarr, 2014] that M_{\max} is perhaps a ubiquitous feature of induced earthquake sequences. Our results here suggest that such a view of M_{\max} —attributable to a finite-sized pressure plume which arrests ruptures that attempt to propagate outside its margins—is only justified in situations where convexity is evident in the magnitude frequency distribution.

We apply our model to a sequence of earthquakes in Arkansas in 2010–2011, likely triggered by wastewater disposal at two nearby wells (section 5). Our calibrated model uses the monthly injection rate at each well, appropriate dimensions for the fault, aquifer and injection well system, and friction and stress parameters established in the earlier simulations. Homogeneous aquifer permeability is estimated to be of order 10^{-13} m², which is constrained by the observed delay between the beginning of injection and the start of seismicity of the Guy-Greenbrier Fault as well as observed pressure buildup around the well. Fault permeability is the main parameter that affects the along-strike migration rate of seismicity on the fault (Figure 12) and we estimate this to be 5×10^{-12} m². Consideration of hypothetical injection scenarios (Figure 13), in which either Well 1 or 5 operates in isolation, suggests that the stacking effect of the two wells is nonlinear in terms of the amount of seismicity triggered. This suggests that interaction between multiple injecting wastewater disposal wells should be considered from an induced seismicity risk perspective.

Appendix A: Bootstrap Sampling of Magnitude Frequency Distribution

The purpose of bootstrap sampling is to construct a stable representation of the magnitude frequency distribution from a catalog of simulated fault ruptures. For a catalog comprising N ruptures, the simplest representation is the cumulative frequency distribution for all events. For instance, for the catalog shown in Figure A1a, where $N=10^4$, this corresponds to the red profile. Because there is an upper magnitude limit, set by the length of the fault, the magnitude frequency distribution curves sharply as it approaches the upper limit, in this case, M_W 4.5. This curvature is a feature of the finite size of the fault, as discussed by Utsu [1999].

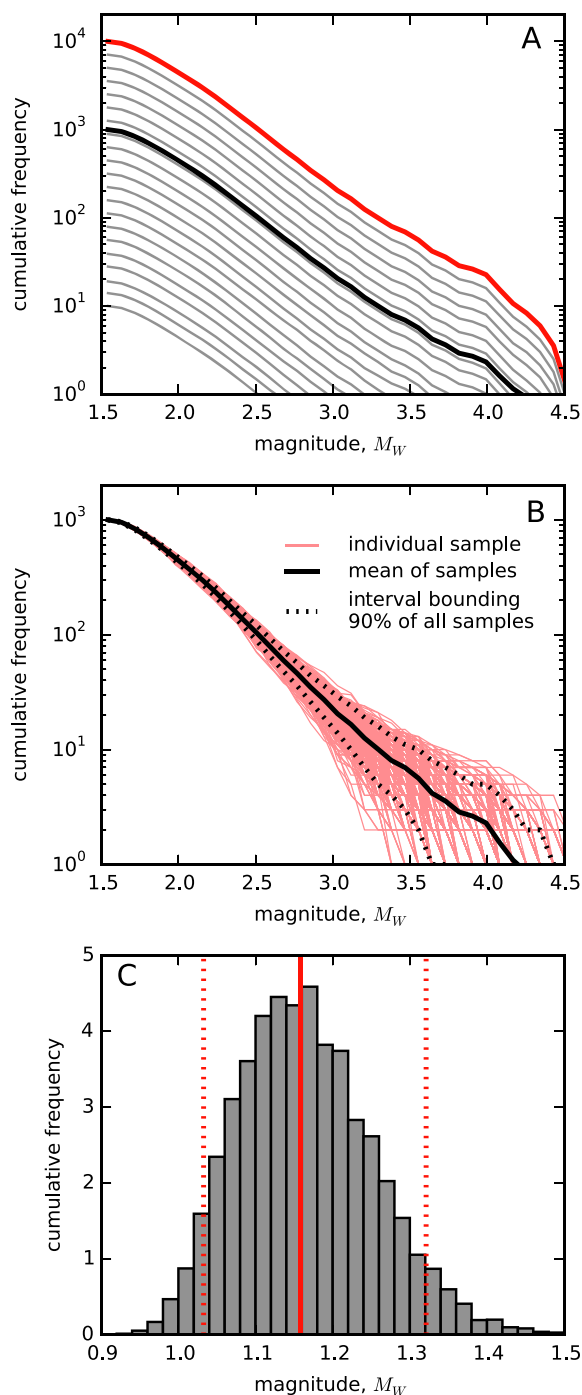


Figure A1. Illustration of bootstrap sampling of magnitude frequency distribution. (a) Average representations of the magnitude frequency distribution for different sample sizes. Note that curvature appears at high magnitude for sample sizes larger than $\sim 10^3$ due to upper magnitude limit M_W 4.5. (b) Red profiles show the magnitude frequency distribution for 1000 randomly drawn samples from catalog TR0. From the samples, a mean profile and the limits of an interval enclosing 90% of samples are calculated. (c) Histogram of b values obtained when fitting a GR model to 10^4 randomly drawn samples from catalog TR0. Median (solid), 5th and 95th percentile values (dashed) are indicated by red lines. This method provides an estimate of the catalog b value and its error.

While such finite fault effects are not a problem in and of themselves—the magnitude frequency distribution can still be characterized by an appropriate nonlinear form of the GR law (e.g., equation (2), see *Utsu* [1999] for others)—they do have the potential to obscure other effects that alter the shape of the magnitude frequency distribution. Therefore, it is useful to consider an average representation of a smaller sub-catalog, comprising $N_{\text{sub}} < N$ ruptures, that does not exhibit the finite fault curvature but still contains essential information such as the b -value. Figure A1a highlights one such representation for $N_{\text{sub}} = 10^3$. Simulations in this paper typically consider catalogs with b values of 1 or higher and resolution of event M_W over a three unit range. Under these conditions, $N_{\text{sub}} = 10^3$ is sufficient to remove the finite fault effect.

A single random draw of N_{sub} events from a catalog comprising N total events yields a magnitude frequency distribution that is sensitive to the statistics of small numbers, particularly at the large-magnitude limit. Therefore, we construct an ensemble of magnitude frequency distributions by taking a large number of random draws, n_{draw} (typically 1000). From the ensemble, we construct both the mean profile as well as the interval enclosing 90% of all profiles (Figure FA1b). For each of the n_{draw} distributions, we estimate (i) a curvature parameter, C_v (see Appendix B) and, if $C_v < 0.45$, (ii) a b value by least squares fitting of a linear curve across the entire magnitude range. An alternative approach to b value estimation is the maximum-likelihood method, however, as our study focuses on qualitative changes in the b value, a least squares fit is sufficient. The distribution of all fitted b values is shown in Figure A1c, and from this we obtain a median, 5th and 95th percentiles as an estimate of the catalog b value and its error. For the catalog shown here, $b = 1.15$ with error interval [1.03, 1.32].

Appendix B: Curvature in Magnitude Frequency Distribution

To assess the adequacy of fitting a GR model to a simulated magnitude frequency distribution, we compute a curvature parameter for the catalog. High curvature

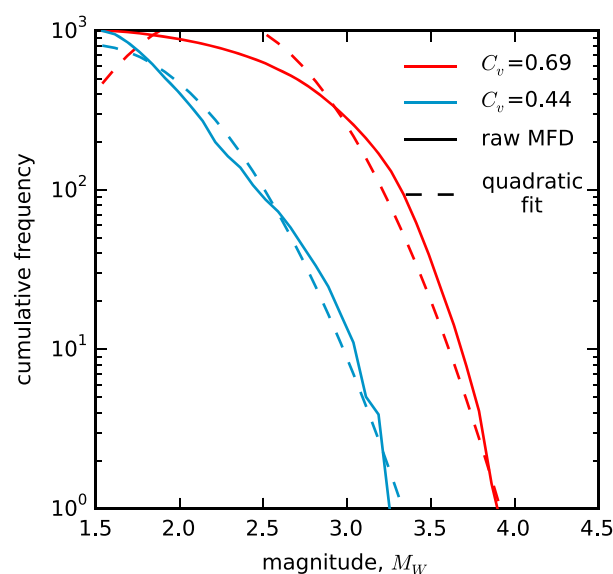


Figure B1. Illustration of quadratic fits (dashed profile) to two simulated magnitude frequency distributions (solid lines, from Figures 7e and 7f. Their associated curvature values, C_v , computed from (B1), are shown.

indicates a departure from linearity and that fitting a GR model is less meaningful. For the simulated magnitude frequency distribution defined at discrete $[M_i, \log(N_i)]$, we use linear regression to find the best fit quadratic function $\log(N) = c_1 M^2 + c_2 M + c_3 = f(M)$. The first curvature, κ_v , [Kreyszig, 1991] and its mean value over the interval $[M_{\min}, M_{\max}]$ is given as

$$\kappa_v = \frac{d^2 f / dM^2}{(1 + (df/dM)^2)^{3/2}}, \quad (B1)$$

$$C_v = \frac{1}{M_{\max} - M_{\min}} \int_{M_{\min}}^{M_{\max}} \kappa_v dM,$$

from which a closed-form expression is obtained in terms of c_1 , c_2 , M_{\max} , and M_{\min} (not quoted here for brevity), satisfying $C_v \rightarrow 0$ as $c_1 \rightarrow 0$.

Figure B1 shows the two simulated magnitude frequency distributions from Figures 7e and 7f, their associated quadratic fits and computed curvatures. Note, this coarse measure of curvature provides no physical meaning but rather is a useful quality factor for determining whether a GR model is an appropriate fit to the data. In this work, we set an arbitrary cutoff of $C_v < 0.45$ for fitting a GR model.

Acknowledgments

Funding for this study was provided by the Stanford Center for Induced and Triggered Seismicity (SCITS). The authors thank E. Dunham and J. Norbeck for helpful discussions and V. Gischig, J. P. Ampuero, M. McClure, and an anonymous reviewer for comments that improved the quality of this article. The data used are listed in the references.

References

- Abercrombie, R. E. (1995), Earthquake source scaling relationships from -1 to 5 ML using seismograms recorded at 2.5 km depth, *J. Geophys. Res.*, *100*, 24,015–24,036.
- Abercrombie, R. E., and J. R. Rice (2005), Can observations of earthquake scaling constrain slip weakening?, *Geophys. J. Int.*, *162*, 406–424.
- Ake, J., K. Mahrer, D. O'Connell, and L. Block (2005), Deep-injection and closely monitored induced seismicity at Paradox Valley, Colorado, *Bull. Seismol. Soc. Am.*, *95*(2), 664–683.
- Aki, K. (1972), Earthquake mechanism, *Tectonophysics*, *13*(1–4), 423–446.
- Albaric, J., V. Oye, N. Langet, M. Hasting, I. Lecomte, K. Iranpour, M. Messeiller, and P. Reid (2014), Monitoring of induced seismicity during the first geothermal reservoir stimulation at Paralana, Australia, *Geothermics*, *52*, 120–131.
- Ampuero, J.-P., and Y. Ben-Zion (2008), Cracks, pulses and macroscopic asymmetry of dynamic rupture on a bimaterial interface with velocity-weakening friction, *Geophys. J. Int.*, *173*, 674–692.
- Ampuero, J.-P., J. Ripperger, and P. M. Mai (2006), Properties of dynamic earthquake ruptures with heterogeneous stress drop, in *Radiated Energy and the Physics of Earthquake Faulting*, *Geophys. Monogr. Ser.*, vol. 70, edited by R. Abercrombie, pp. 3–13, AGU, Washington, D. C.
- Andrews, D. J. (1980), A stochastic fault model 1. Static case, *J. Geophys. Res.*, *85*(B7), 3867–3877.
- Bachmann, C. E., S. Wiemer, B. P. Goertz-Allmann, and J. Woessner (2012), Influence of pore-pressure on the event-size distribution of induced earthquakes, *Geophys. Res. Lett.*, *39*, L09302, doi:10.1029/2012GL051480.
- Barton, C. A., M. D. Zoback, and D. Moos (1995), Fluid flow along potentially active faults in crystalline rock, *Geology*, *23*(8), 683–686.
- Ben-Zion, Y., M. Eneva, and Y. Liu (2003), Large earthquake cycles and intermittent criticality on heterogeneous faults due to evolving stress and seismicity, *J. Geophys. Res.*, *108*(B6), 2307, doi:10.1029/2002JB002121.
- Brodsky, E. E., and L. J. Lajoie (2013), Anthropogenic seismicity rates and operational parameters at the Salton Sea Geothermal Field, *Science*, *341*(543), 543–546.
- Bromley, C. J., C. F. Pearson, D. M. Rigor Jr., and PNOG-EDC (1987), Microearthquakes at the Puhagan geothermal field, Philippines—A case of induced seismicity, *J. Volcanol. Geotherm. Res.*, *31*, 293–311.
- Causse, M., L. A. Dalguer, and P. M. Mai (2013), Variability of dynamic source parameters inferred from kinematic models of past earthquakes, *Geophys. J. Int.*, *196*, 1754–1769, doi:10.1093/gji/ggt478.
- Cesca, S., F. Grigoli, S. Heimann, Á. González, E. Buforn, S. Maghsoudi, E. Blanch, and T. Dahm (2014), The 2013 September–October seismic sequence offshore Spain: A case of seismicity triggered by gas injection?, *Geophys. J. Int.*, *198*, 941–953.
- Cornell, C. A. (1968), Engineering seismic risk analysis, *Bull. Seismol. Soc. Am.*, *58*(5), 1583–1606.
- Dempsey, D. and J. Suckale (2016), Collective properties of injection-induced earthquake sequences: 1. Model description and directivity bias, *J. Geophys. Res. Solid Earth*, *121*, doi:10.1002/2015JB012550.
- Dempsey, D., S. Kelkar, R. Pawar, E. Keating, and D. Coblentz (2014), Modeling caprock bending stresses and their potential for induced seismicity during CO₂ injection, *Int. J. Greenhouse Gas Control*, *22*, 223–236.
- Dempsey, D., S. Kelkar, N. Davatzes, S. Hickman, and D. Moos (2015), Numerical modeling of injection, stress and permeability enhancement during shear stimulation at the Desert Peak Enhanced Geothermal System, *Int. J. Rock Mech. Min. Sci.*, *78*, 190–206.
- Dorbath, L., N. Cuenot, A. Genter, and M. Frogneux (2009), Seismic response of the fractured and faulted granite of Soultz-sous-Forêts (France) to 5 km deep massive water injections, *Geophys. J. Int.*, *177*, 653–675.

- El-Isa, Z. H., and D. W. Eaton (2014), Spatiotemporal variations in the b -value of earthquake magnitude-frequency distributions: Classification and causes, *Tectonophysics*, *615*, 1–11.
- Eshelby, J. D. (1957), The determination of the elastic field of an ellipsoidal inclusion, and related problems, *Proc. R. Soc. A*, *241*, 376–391.
- Eshelby, J. D. (1969), The elastic field of a crack extending non-uniformly under general anti-plane loading, *J. Mech. Phys. Solids*, *17*, 177–199.
- Fletcher, J. B., and L. R. Sykes (1977), Earthquakes related to hydraulic mining and natural seismic activity in western New York State, *J. Geophys. Res.*, *82*(26), 3767–3780.
- Friberg, P. A., G. M. Besana-Ostman, and I. Dricker (2014), Characterization of an earthquake sequence triggered by hydraulic fracturing in Harrison County, Ohio, *Seismol. Res. Lett.*, *85*(6), doi:10.1785/0220140127.
- Frohlich, C., C. Hayward, B. Stump, and E. Potter (2011), The Dallas-Fort worth earthquake sequence: October 2008 through May 2009, *Bull. Seismol. Soc. Am.*, *101*(1), 327–340.
- Gibbs, J. F., J. H. Healy, C. B. Raleigh, and J. Coakley (1973), Seismicity in the Rangely, Colorado, area: 1962–1970, *Bull. Seismol. Soc. Am.*, *63*(5), 1557–1570.
- Gischig, V. (2015), Rupture propagation behavior and the largest possible earthquake induced by fluid injection into deep reservoirs, *Geophys. Res. Lett.*, *42*, 7420–7428, doi:10.1002/2015GL065072.
- Gischig, V., and S. Wiemer (2013), A stochastic model for induced seismicity based on non-linear pressure diffusion and irreversible permeability enhancement, *Geophys. J. Int.*, *194*, 1229–1249, doi:10.1093/gji/ggt164.
- Goebel, T. H. W., S. M. Hosseini, F. Cappa, E. Hauksson, J. P. Ampuero, F. Aminzadeh, and J. B. Saleeby (2016), Wastewater disposal and earthquake swarm activity at the southern end of the Central Valley, California, *Geophys. Res. Lett.*, *43*, 1092–1099, doi:10.1002/2015GL066948.
- Goertz-Allmann, B. P., and S. Wiemer (2013), Geomechanical modeling of induced seismicity source parameters and implications for seismic hazard assessment, *Geophysics*, *78*(1), KS25–KS39, doi:10.1190/GEO2012-0102.1.
- Goertz-Allmann, B. P., A. Goertz, and S. Wiemer (2011), Stress drop variations of induced earthquakes at the Basel geothermal site, *Geophys. Res. Lett.*, *38*, L09308, doi:10.1029/2011GL047498.
- Goertz-Allmann, B. P., D. Kühn, V. Oye, B. Bohloli, and E. Aker (2014), Combining microseismic and geomechanical observations to interpret storage integrity at the In Salah CCS site, *Geophys. J. Int.*, *198*, 447–461, doi:10.1093/gji/ggu010.
- Guest, A., E. Rebel, S. M. Bailly, and J. Kostadinovic (2014), Integrated analysis for fracture identification during hydraulic fracturing, paper SPE-170714-MS presented at SPE Annual Technical Conference and Exhibition, Society of Petroleum Engineers, Amsterdam, Netherlands, 27–29 Oct.
- Hanks, T. C., and H. Kanamori (1979), A moment magnitude scale, *J. Geophys. Res.*, *84*, 2348–2350.
- Häring, M. O., U. Schanz, F. Ladner, and B. C. Dyer (2008), Characterisation of the Basel 1 enhanced geothermal system, *Geothermics*, *37*, 469–494.
- Healy, J. H., W. W. Rubey, D. T. Griggs, and C. B. Raleigh (1968), The Denver earthquakes, *Science*, *161*(3848), 1301–1310.
- Holland, A. A. (2013), Earthquakes triggered by hydraulic fracturing in South-Central Oklahoma, *Bull. Seismol. Soc. Am.*, *103*(3), 1784–1792.
- Horton, S. (2012), Disposal of hydrofracking waste fluid by injection into subsurface aquifers triggers earthquake swarm in Central Arkansas with potential for damaging earthquake, *Seismol. Res. Lett.*, *83*(2), 250–260.
- Huang, Y., and G. C. Beroza (2015), Temporal variation in the magnitude-frequency distribution during the Guy-Greenbrier earthquake sequence, *Geophys. Res. Lett.*, *42*, 6639–6646, doi:10.1002/2015GL065170.
- Huang, J., and D. L. Turcotte (1988), Fractal distributions of stress and strength and variations of b -value, *Earth Planet. Sci. Lett.*, *91*, 223–230.
- Kammer, D. S., M. Radiquet, J.-P. Ampuero, and J.-F. Molinari (2015), Linear elastic fracture mechanics predicts the propagation distance of frictional slip, *Tribol. Lett.*, *57*(3), 23, doi:10.1007/s11249-014-0451-8.
- Keränen, K. M., H. M. Savage, G. A. Abers, and E. S. Cochran (2013), Potentially induced earthquakes in Oklahoma, USA: Links between wastewater injection and the 2011 M_w 5.7 earthquake sequence, *Geology*, *41*(6), 699–702.
- Kreyszig, E. (1991), *Differential Geometry*, Dover, New York.
- Lei, X., G. Yu, S. Ma, X. Wen, and Q. Wang (2008), Earthquakes induced by water injection at ~3 km depth within the Rongchang gas field, Chongqing, China, *J. Geophys. Res.*, *113*, B10310, doi:10.1029/2008JB005604.
- Lei, X., S. Ma, W. Chen, C. Pang, J. Zeng, and B. Jiang (2013), A detailed view of the injection-induced seismicity in a natural gas reservoir in Zigong, southwestern Sichuan Basin, China, *J. Geophys. Res. Solid Earth*, *118*, 4296–4311, doi:10.1002/jgrb.50310.
- Lengliné, O., L. Lamourette, L. Vivin, N. Cuenot, and J. Schmittbuhl (2014), Fluid-induced earthquakes with variable stress drop, *J. Geophys. Res. Solid Earth*, *119*, 8900–8913, doi:10.1002/2014JB011282.
- Llenos, A. L., and A. J. Michael (2013), Modeling earthquake rate changes in Oklahoma and Arkansas: Possible signatures of induced seismicity, *Bull. Seismol. Soc. Am.*, *103*(5), 2850–2861.
- Madariaga, R. (1979), On the relation between seismic moment and stress drop in the presence of stress and strength heterogeneity, *J. Geophys. Res.*, *84*(B5), 2243–2250.
- Mai, P. M., and G. C. Beroza (2002), A spatial random field model to characterize complexity in earthquake slip, *J. Geophys. Res.*, *107*(B11), 2308, doi:10.1029/2001JB000588.
- McClure, M. W., and R. N. Horne (2011), Investigation of injection-induced seismicity using a coupled fluid flow and rate/state friction model, *Geophysics*, *76*(6), WC181–WC198, doi:10.1190/GEO2011-0064.1.
- McGarr, A. (2014), Maximum magnitude earthquakes induced by fluid injection, *J. Geophys. Res. Solid Earth*, *119*, 1008–1019, doi:10.1002/2013JB010597.
- Murphy, S., G. S. O'Brien, J. McCloskey, C. J. Bean, and S. Nalbant (2013), Modelling fluid induced seismicity on a nearby active fault, *Geophys. J. Int.*, *194*, 1613–1624.
- Peaceman, D. W. (1983), Interpretation of well-block pressures in numerical reservoir simulation with nonsquare grid blocks and anisotropic permeability, *Soc. Pet. Eng. J.*, *23*(3), 531–543.
- Raleigh, C. B., J. H. Healy, and J. D. Bredehoeft (1976), An experiment in earthquake control at Rangely, Colorado, *Science*, *191*(4233), 1230–1237.
- Ripperger, J., J.-P. Ampuero, P. M. Mai, and D. Giardini (2007), Earthquake source characteristics from dynamic rupture with constrained stochastic fault stress, *J. Geophys. Res.*, *112*, B04311, doi:10.1029/2006JB004515.
- Scholz, C. H. (1968), The frequency-magnitude relation of microfracturing in rock and its relation to earthquakes, *Bull. Seismol. Soc. Am.*, *58*(1), 399–415.
- Schorlemmer, D., S. Wiemer, and M. Wyss (2005), Variations in earthquake-size distribution across different stress regimes, *Nature*, *437*, 539–542.
- Shapiro, S. A., E. Huenges, and G. Borm (1997), Estimating the crust permeability from fluid-injection-induced seismic emission at the KTB site, *Geophys. J. Int.*, *131*, 15–18.

- Shapiro, S. A., O. S. Krüger, C. Dinske, and C. Langenbruch (2011), Magnitudes of induced earthquakes and geometric scales of fluid-stimulated rock volumes, *Geophysics*, *76*(6), WC55–WC63, doi:10.1190/GEO2010-0349.1.
- Skoumal, R. J., M. R. Brudzinski, and B. S. Currie (2015), Earthquakes induced by hydraulic fracturing in Poland Township, Ohio, *Bull. Seismol. Soc. Am.*, *105*(1), 189–197, doi:10.1785/0120140168.
- Smith, W. (1981), The *b*-value as an earthquake precursor, *Nature*, *289*, 136–139.
- Smith, D. E., and T. H. Heaton (2011), Models of stochastic, spatially varying stress in the crust compatible with focal-mechanism data, and how stress inversions can be biased toward the stress rate, *Bull. Seismol. Soc. Am.*, *101*(3), 1396–1421.
- Utsu, T. (1999), Representation and analysis of the earthquake size distribution: A historical review and some new approaches, *Pure Appl. Geophys.*, *155*, 509–535.
- Vermilyen, J., and M. D. Zoback (2011), Hydraulic fracturing, microseismic magnitudes, and stress evolution in the Barnett Shale, Texas, USA, paper SPE-140507-MS presented at SPE Hydraulic Fracturing Conference, Society of Petroleum Engineers, The Woodlands, Tex., 24–26 Jan.
- Vidale, J. E., D. C. Agnew, M. J. S. Johnston, and D. H. Oppenheimer (1998), Absence of earthquake correlation with Earth tides: An indication of high preseismic fault stress rate, *J. Geophys. Res.*, *103*(B10), 24,567–24,572.
- Zhou, R., G. D. Huang, P. Snelling, M. P. Thornton, and M. Mueller (2013), Magnitude calibration for microseismic events from hydraulic fracture monitoring, paper SEG-2013-0648 presented at SEG Annual Meeting, Society of Exploration Geophysicists, Houston, Tex., 22–27 Sept.
- Zoback, M. D., and S.-M. Gorelick (2012), Earthquake triggering and large-scale geologic storage of carbon dioxide, *Proc. Natl. Acad. Sci. U.S.A.*, *109*(26), 10,164–10,168.
- Zoback, M. D., and H.-P. Harjes (1997), Injection-induced earthquakes and crustal stress at 9 km depth at the KTB deep drilling site, Germany, *J. Geophys. Res.*, *102*(B8), 18,477–18,491.
- Zoback, M. D., and M.-L. Zoback (1991), Tectonic stress field of North America and relative plate motions, in *Neotectonics of North America*, edited by D. B. Slemmons, pp. 339–366, Geol. Soc. Am., Denver, Colo.
- Zöller, G., M. Holschneider, and Y. Ben-Zion (2005), The role of heterogeneities as a tuning parameter of earthquake dynamics, *Pure Appl. Geophys.*, *162*, 1027–1049.
- Zyvoloski, G. A. (2007), FEHM: A control volume finite element code for simulating subsurface multi-phase multi-fluid heat and mass transfer, *LAUR-07-3359*.